

Jacob Rosen • Blake Hannaford  
Richard M. Satava  
Editors

# Surgical Robotics

Systems Applications and Visions

 Springer

*Editors*

Jacob Rosen  
Department of Computer Engineering  
Jack Baskin School of Engineering  
University of California Santa Cruz  
1156 High Street, Santa Cruz  
CA 95064, USA  
rosen@ucsc.edu

Blake Hannaford  
Department of Electrical Engineering  
University of Washington  
Box 325500, Seattle  
Washington 98195-2500  
USA  
hannaford@ee.washington.edu

Richard M. Satava  
Department of Surgery  
University of Washington Medical Center  
Box 356410  
1959 Pacific Street NE, Seattle  
Washington 98195, USA  
rsatava@u.washington.edu

ISBN 978-1-4419-1125-4                      e-ISBN 978-1-4419-1126-1  
DOI 10.1007/978-1-4419-1126-1  
Springer New York Dordrecht Heidelberg London

© Springer Science+Business Media, LLC 2011

All rights reserved. This work may not be translated or copied in whole or in part without the written permission of the publisher (Springer Science+Business Media, LLC, 233 Spring Street, New York, NY 10013, USA), except for brief excerpts in connection with reviews or scholarly analysis. Use in connection with any form of information storage and retrieval, electronic adaptation, computer software, or by similar or dissimilar methodology now known or hereafter developed is forbidden.

The use in this publication of trade names, trademarks, service marks, and similar terms, even if they are not identified as such, is not to be taken as an expression of opinion as to whether or not they are subject to proprietary rights.

Printed on acid-free paper

Springer is part of Springer Science+Business Media ([www.springer.com](http://www.springer.com))

## Chapter 24

# Macro and Micro Soft-Tissue Biomechanics and Tissue Damage: Application in Surgical Robotics

Jacob Rosen, Jeff Brown, Smita De, and Blake Hannaford

**Abstract** Accurate knowledge of biomechanical characteristics of tissues is essential for developing realistic computer-based surgical simulators incorporating haptic feedback, as well as for the design of surgical robots and tools. Most past and current biomechanical research is focused on soft and hard anatomical structures that are subject to physiological loading while testing the organs in situ. Internal organs are different in that respect since they are not subject to extensive loads as part of their regular physiological function. However, during surgery, a different set of loading conditions are imposed on these organs as a result of the interaction with the surgical tools. The focus of the current study was to obtain the structural biomechanical properties (engineering stress-strain and stress relaxation) of seven abdominal organs, including bladder, gallbladder, large and small intestines, liver, spleen, and stomach, using a porcine animal model. The organs were tested in vivo, in situ, and ex corpus (the latter two conditions being postmortem) under cyclical and step strain compressions using a motorized endoscopic grasper and a universal-testing machine. The tissues were tested with the same loading conditions commonly applied by surgeons during minimally invasive surgical procedures. Phenomenological models were developed for the various organs, testing conditions, and experimental devices. A property database—unique to the literature—has been created that contains the average elastic and relaxation model parameters measured for these tissues in vivo and postmortem. The results quantitatively indicate the significant differences between tissue properties measured in vivo and postmortem. A quantitative understanding of how the unconditioned tissue properties and model parameters are influenced by time postmortem and loading condition has been obtained. The results provide the material property foundations for developing science-based haptic surgical simulators, as well as surgical tools for manual and robotic systems.

---

© 2008 ASME. Reprinted, with permission, from, Biomechanical Properties of Abdominal Organs In Vivo and Postmortem under Compression Loads, by Rosen Jacob, Jeffrey D. Brown, Smita De, Mika N. Sinanan Blake Hannaford. That was published in: ASME Journal of Biomedical Engineering, vol. 130, Issue 2, April 2008

J. Rosen (✉)

Department of Computer Engineering, Jack Baskin School of Engineering,  
University of California Santa Cruz, 1156 High street, Santa Cruz, CA 95064-1099, USA  
e-mail: rosen@ucsc.edu

**Keywords** Soft tissue · Biomechanics · Internal organs · Surgical robotics · Surgical simulation · Haptics · Surgical tools

## 24.1 Introduction

New technologies have fundamentally changed the practice of surgery. Having recently introduced minimally invasive (laparoscopic) techniques, surgery is now poised to take another big step by incorporating surgical robotic systems into practice. These robotic devices [1] are only in their first generation of development but promise to significantly improve surgical dexterity in small and remote body cavities. Along with surgical robots, surgical simulators are being introduced into the curriculum for surgical training. To perform or simulate manipulation of soft tissues, both surgical robots and surgical simulators must be engineered with knowledge of the biomechanical properties of the tissues most relevant to the clinical application. To date, there have been little biomechanical data available, and current simulators and robots have largely been engineered to accomplish acceptable “handling” characteristics, as determined by expert surgeon consultants. While the initial pioneering surgical robots from Intuitive Surgical and Computer Motion, Inc. (now merged) have achieved FDA approval and some commercial success without detailed biomechanical data, as this field matures, the need for precise instrument design based on quantitative evaluation of tissue biomechanical properties will increase. Accurate models of clinically relevant tissues will allow designers to predict manipulation forces and torques required. The first step to understanding the consequences of tissue stress is a better understanding of the biomechanics of the tissues.

Surgical training has been affected by many factors such as statutory limitation of work hours, patient safety concerns, and a growing regulatory push for credentialing of surgical trainees. Formal curriculum development with specific milestones and significant improvement in computer-based surgical simulation as a training tool have also augmented the surgical armamentarium. However, initial simulation efforts did not focus on the accuracy with which they render deformation forces and displacements of the tissues and few provided any haptic feedback. As the next generation of simulators are developed, biomechanical data are essential for making this feedback accurate. The consequences of inaccurate tissue deformation modeling on clinical performance after simulation training has not been formally studied, but it is reasonable to imagine that students accustomed to inaccurate forces or displacements from simulation training might be at greater risk of tissue injury when applying their clinical skills in the actual operating room.

With few exceptions, most of the existing literature on the biomechanics of internal organ tissue comes from measurements taken from non-living tissue. Often the tissue has been frozen and thawed for convenient laboratory use. Physiologic changes in living tissue certainly influence the mechanical properties of soft tissues

in-vivo. Another issue is the effect of fluid within the tissue. For example, after several similar loading cycles, the non-linear stiffness and hysteresis of soft tissues typically stabilizes – a phenomenon known as conditioning [2]. Most researchers “precondition” their tissue samples to obtain consistent results by cycling them 10–20 times before collecting data. This process runs counter to the normal conditions found in surgery since surgeons do not precondition tissues before manipulating them. “First squeeze” behavior of tissues has not been widely reported.

In 1967, Fung published classic work on rabbit mesentery in uni-axial tension [3]. Yamada in 1973 reported results of tests on esophagus, stomach, small and large intestines, liver, and gallbladder [4]. Much of this work was done with animal organs in-vitro, but some data was presented from human cadavers. Most of the data were expressed as tissue tension with an emphasis on measurement of failure levels.

A large literature describes testing abdominal organs in relation to blunt impact injury, especially in the context of automobile accidents. Yoganandan et al. (2001) and Rouhana (1993) reviewed many of these studies [5, 6]. More detailed measurements of specific organs include shear measurements of liver [7–9], and distension of intestine (relation between pressure and volume) [10, 11].

In the context of laparoscopic surgery, Carter et al. [12] measured the uniaxial force required to puncture pig and sheep livers with a scalpel as well as the displacement of the tissue when puncture occurred. Other studies by these researchers [13, 14] used a bench-top device in ex-corpore testing of pig and sheep liver and spleen. They also performed in-vivo measurements reviewed below. Tamura et al. [15] studied porcine liver, spleen, and kidney in-vitro by compression loading of rectangular-shaped samples. Elastic and stress relaxation properties were examined, but the nature of the studies – single-point displacement of small fragments of tissue – limit application to clinical conditions.

In an effort to improve the physiological accuracy of ex-corpore testing, some studies have used perfusion of the excised organ. Davies et al. [14] tested artificially perfused spleen, while Melvin et al. (1973) [16] placed intact kidney and liver into a uni-axial compression testing machine while still perfused by the body. The emphasis was on measurement of tissue failure (as low as 293kPa for liver). Other interesting in-vivo results have been obtained in research on prosthetics [17–19]. Zheng et al. (1999) used a combination of load cell and ultrasound to measure compressive properties non-invasively [17, 18]. However, this method requires a rigid backing, such as bone.

Brouwer et al. [20] developed several instruments for tensile and compressive testing of porcine tissues in-vitro and in-vivo. One of these devices contained two grippers whose separation was controlled by a lead-screw and stepper motor. Ottensmeyer and Salisbury [21] developed the TeMpEST 1-D device which applies high frequency, low amplitude compressive displacements to the surface of an organ. In-vivo testing with this device showed a relationship between elastic modulus and frequency. Carter et al. [13] used a similar hand-held indentation device and recorded the only published in-vivo data obtained from living human subjects. Maximum applied strain was 60kPa. Interestingly, diseased liver was at least twice as stiff

as normal, which supports the clinical surgical impression. Kalanovic et al. [22] developed a rotary shear device (ROSA-2), which used a 6mm right cylindrical contact surface that rotates relative to a fixed outer ring. Slippage was prevented by a needle array or cyanoacrylate adhesive. Calculated material parameters agreed in the range of 0–10 Hz with those found with the TeMpEST 1-D.

In a departure from prior studies with specialized stress-strain measurement devices, Bicchi et al. [23] applied sensors to standard surgical tools, in this case adding force and position sensors to measure jaw force and angle in endoscopic surgical pliers. Morimoto et al. [24] instrumented a laparoscopic Babcock grasper with a six-axis force/torque sensor to record forces and torques applied during animal procedures. Their device successfully isolated tool-tissue interaction forces from forces arising from the abdominal wall and port. Brouwer et al. [20] used a six-axis force/torque sensor mounted to a modified grasper to measure the forces and torques applied to the tool while driving a needle through porcine abdominal tissues. Greenish et al. [25] instrumented scissors to collect in-situ data during cutting of skin, abdominal wall, muscle, and tendon tissues from sheep and rats.

Building on this experience, our group has developed a series of devices for measurement of tool-tissue interactions during surgery. We have developed a laparoscopic tissue grasper with six-axis force/torque and grasp force-sensing capability embedded in an articulated mechanism for measurement of motion in five axes (the “Blue DRAGON” system) [26–28]. The devices described above were passive, or human-powered, and were used for measurement of activity during simulated surgical procedures. For example, two of the Blue DRAGON devices were used on the left and right hand tools in experiments recording a database from 30 surgeons performing portions of a laparoscopic cholecystectomy (gallbladder removal) and gastric fundoplication (antireflux surgery) in pigs [83]. We have also developed and evaluated several motorized and teleoperated graspers, including the Force-Reflecting Endoscopic Grasper (FREG) [36]. Active, or motorized, tools facilitate the application of controlled displacements or forces to tissue under computer control. The FREG was used [29] to test several porcine liver, spleen, stomach, small and large intestine, and lung specimens in-vivo and measure their force-displacement response to stresses up to 100kPa and compressive strains up to 60%. The measured force-deformation responses could be fit with an exponential function, resulting in two coefficients that could differentiate the tissues.

Based on data collected with the Blue DRAGON system, the Motorized Endoscopic Grasper (MEG) was designed to reproduce the maximum grasping forces and velocities observed during clinical surgical tissue manipulation and acquire more extensive and reliable compressive data from abdominal organs [30, 31]. Full characterization of a non-linear, fluid-perfused, non-isotropic and non-homogeneous material such as the major internal organs is a complex endeavor. To name just one difficulty, proper modeling of bulk materials requires knowledge from tri-axial testing that can only come from tissue biomechanical studies that are not similar to surgical conditions. Although in general it will not be possible to fully characterize these materials with the uni-axial compressive tests our instrument can perform, we must begin to measure at least basic in-vivo properties.

The emphasis in this paper is on the devices and methodology for collection of tissue performance data rather than tissue modeling. For clarity, a few curves were fit to the data and have been included. A more complete description of tissue models derived from these data are provided in a companion paper [32].

There is substantial literature on mathematical models for the response of soft tissue to mechanical testing. Fung [2] noted that many tissues seem to follow an exponential relationship between stress and strain. Soft tissues also exhibit hysteresis between loading and unloading. The loading and unloading curves are generally different, and we will concentrate on the loading curve only (pseudo-elasticity). For example, Brouwer et al. [20] fit their data to Fung's exponential curve. A similar procedure was used by Rosen et al. [29] and Tamura et al. [15].

There are many approaches for modeling the time-dependent response of soft tissues, including Quasi-Linear Viscoelasticity (QLV) [2, 33, 34], bi-phasic models [35–41], and even tri-phasic theory [42] involving solid, fluid, and ionic concentration state variables. While there is much potential to apply sophisticated time-dependent models to our data, at this point we will limit ourselves to simply fitting our data with first order exponential time functions.

As indicated in this literature review, biomechanical properties were studied at the macro scale level in selected well controlled experimental conditions, however little is known about the types of stresses that can be safely applied using surgical instruments while limiting tissue damage and potentially injury. In earlier work with the porcine animal model, we measured relationships between acute indicators of tissue injury and average surgical grasping stress [47]. In these experiments, tissue damage was observed even at low average grasping forces, suggesting that the observed tissue damage might correspond to the spatial stress distribution between the grasper jaws instead of average stress.

It is evident from the literature that four things are lacking for modeling tissues in the context of surgery: (1) an understanding of how surgeons interact with tissues (i.e., to establish the relevant scale of stress and strain), (2) compression testing, (3) in-vivo data, and (4) human data (5) an understanding of tissue damage at the cellular level as well as the relationship between the stress developed at the tissue and acute tissue injury. Most studies have tested tissues in-vitro in tension using excised animal specimens (often after freezing and thawing).

## **24.2 Methods**

### ***24.2.1 Macro Scale Biomechanics***

#### **24.2.1.1 Definitions**

In this study, in-vivo will refer to testing done inside an intact live specimen, with the organ in its normal position. In-situ will refer to testing the same organs after the

animal has died, but with the organs still in the body proper. In-vitro refers to testing done outside the body, using tissue samples that have been excised from the bulk organ. Finally, *ex-corpore* will refer to intact, non-living organs removed from the body, and possibly stored before testing some time postmortem.

#### 24.2.1.2 Tools

Two types of tools were used to acquire the biomechanical properties of internal organs in-vivo, in-situ and *ex-corpore*: (1) a custom-made motorized endoscopic grasper (MEG), used in all conditions; and (2) a servohydraulic universal testing material testing system by MTS Corporation (Eden Prairie, Minnesota), used for testing tissue only *ex-corpore* only.

#### 24.2.1.3 Motorized Endoscopic Grasper

The motorized endoscopic grasper is the second generation of Force-Reflecting Endoscopic Grasper (FREG) [29] that was originally designed as a 1 degree-of-freedom (DOF), bi-lateral teleoperated system, but was also capable of applying in-vivo computer controlled sequences of compressive force via a flat-coil actuated endoscopic grasper (slave element). As such, it was used to test several porcine abdominal tissues in-vivo to measure their stress-strain response but could only apply approximately 8N compressive force that was estimated by measuring the current to the flat-coil actuator. Following these research efforts the Motorized Endoscopic Grasper (MEG) was designed to further examine the compressive properties of porcine abdominal organs [30, 31]. The engineering specifications of the MEG were based on data collected from previous experiments using the Blue DRAGON surgical tool tracking system [43]. These data were examined in order to determine the forces, deformations, and timing of compressive loads applied on tissues.

The MEG uses a brushed DC motor (RE25, 10W, Maxon Precision Motors – Fall River, MA) with a 19:1 planetary gearhead (GP26, Maxon Precision Motors – Fall River, MA) to drive a Babcock grasper (#33510 BL, Karl Storz – Germany) – Fig. 24.1. The motor is attached to a capstan that drives a cable and partial pulley. The pulley is attached to a cam joint that converts the rotational motion of the motor and pulley to a linear translation of the grasper shaft, which opens and closes the jaws. A 500-count digital encoder (HEDL55, Hewlette-Packard – Palo Alto, CA), attached to the motor, measures angular position. The mechanism's overall effective gearing ratio is approximately 190:1, including the planetary gearhead ratio (19:1) and the partial pulley-capstan gearing ratio (10:1), increasing the 29 mNm of continuous torque generated by the motor to 5.51Nm applied by the partial pulley. A wide variety of standard Karl Storz laparoscopic instruments can be attached to the base plate mount, but a Babcock grasper (Fig. 24.1c) was selected as the primary loading device due to its special geometry. Range of motion for the Babcock jaws is 54.3 deg,

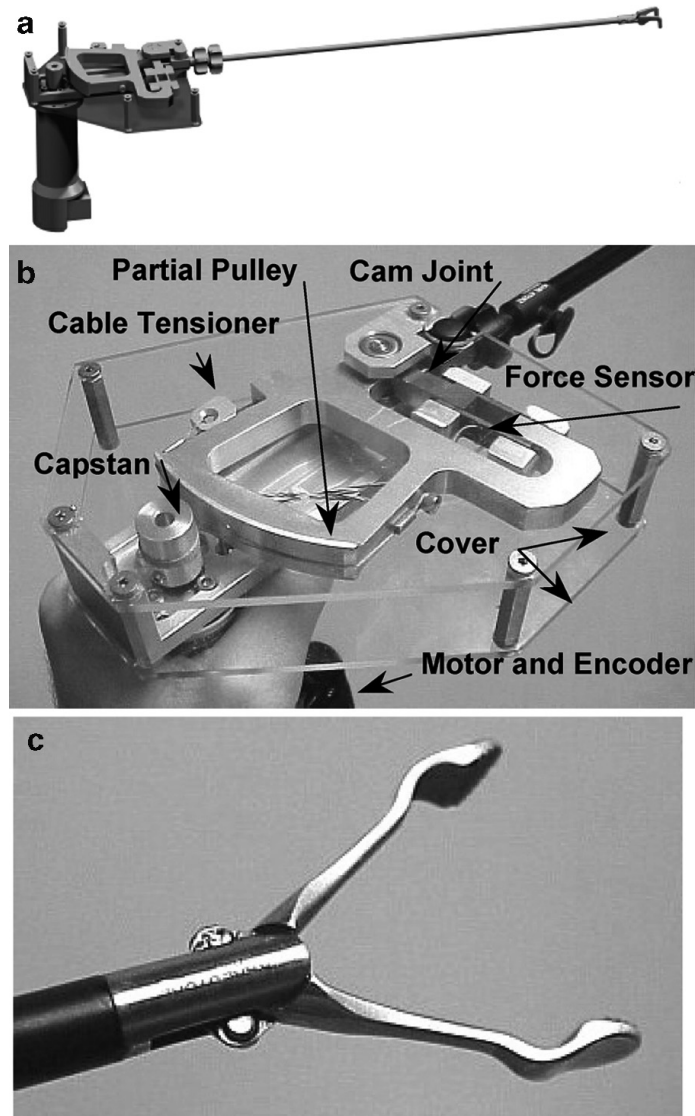


**Fig. 24.1** The Motorized Endoscopic Grasper (MEG): (a) rendered CAD drawing of MEG (protective top cover not shown), (b) close-up photograph of the MEG's drive mechanism, (c) close-up photograph of the MEG's Babcock grasper end effector

or 184 deg at the capstan. Resolution of jaw angle is approximately  $1.13 \times 10^{-2}$  deg per encoder count ( $5.5 \times 10^{-3}$  mm at the jaws' grasping surfaces). At full opening, the two grasping surfaces are 26.3 mm apart.

A double-beam planar force sensor (FR1010, 40 lb, Futek – Irvine, CA) is mounted in the partial pulley, measuring force applied to the end effector. The signals are amplified with a Futek signal conditioning unit (model JM-2). The resolution of force signals following a 16-bit A/D conversion is 0.6 mN. A noise level of up to 50 mN, including the quantization noise, was observed, which represents 0.025% of the sensor's full scale. The maximum continuous motor torque of 29 mNm is equivalent to 26.5 N of grasping force by the Babcock grasper's jaws, after transmission through the mechanism, which is greater than the

average force applied by surgeons during typical surgical tasks [43]. Based on the Babcock grasper's jaw dimensions, the application of 26.5 N is equivalent to a compressive stress of 470 kPa. The MEG is hand-held and weighs 0.7 kg. It is inserted into the body through standard 10mm endoscopic "ports" used for passing videoendoscopic instruments into the body without losing the gas pressure in the abdomen.

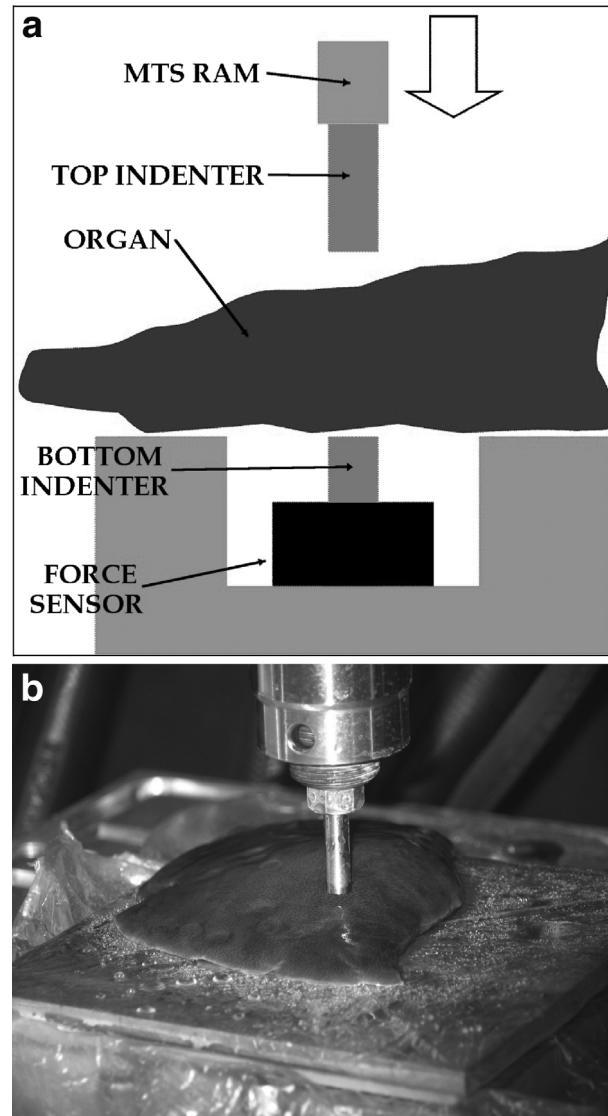
Computer control of the MEG is provided via a PC using a proportional-derivative (PD) position controller implemented in Simulink (Mathworks – Natick, MA) and dSPACE (Novi, MI) user interface software (ControlDesk) and hardware (DS1102). Current is supplied to the motor via a voltage-controlled current supply (escap ELD-3503, Portescap – Hauppauge, NY) controlled by the output from the dSPACE board (D/A 16-bit). The control loop runs at 1kHz. The MEG was calibrated to address the nonlinear relationship between the position of and the force applied by the distal tool tips with respect to the sensors located on the proximal end of the tool (defined analytically in [29]), as well as to compensate for mechanism compliance and backlash.

#### 24.2.1.4 MTS Setup

The testing system by MTS Corporation is a standard servo-hydraulic universal-testing machine often used in material testing in the field of biomechanics. The custom-built frame was used with a model 252 valve. Maximum closed-loop velocity of the ram using this valve is 500 mm/s.

The experimental setup used with the MTS machine for tissue testing is shown in Fig. 24.2. The top and bottom indenters were identical 7 mm diameter right circular cylinders providing a contact area of 38.5 mm<sup>2</sup>, compared to the MEG's contact area of 56.4 mm<sup>2</sup>. The top indenter screwed into the MTS ram (the moving portion of the machine). The bottom indenter was fixed to the tension/compression force sensor (44.5N tension/compression unit, Sensotec model #31/1426-04). The force sensing resolution was 21.7m N. A noise level of up to 9m N including the quantization noise, was observed, which represents 0.019% of the sensor's full scale. The force sensor rested in a stainless steel base plate that was affixed to the MTS frame. The top of the base plate and the top of the bottom indenter were aligned. The organ rested on the base plate and the bottom indenter. The opening was just large enough to accommodate the force sensor but not allow the tissue to droop significantly. Additionally, the base plate had two grooves, one vertical slot for routing the force sensor's wire and the other a horizontal one around the entire base for cinching down a very thin plastic sheet with a rubber band. This plastic sheet protected the force sensor from fluids present during testing. Despite the presence of this sheet and the fact that the effective top of the force sensor and the rest of the plate were level, it was assumed that the force sensor would measure the majority of the applied pressure, since the film was very thin and flexible and there was a relatively large gap surrounding the force sensor indenter (Fig. 24.2).

**Fig. 24.2** MTS experimental testing machine setup: (a) schematic overview of the system, (b) the setup with a liver ex-corpous



The MTS ram was operated in a position-control mode using TestStar II software and hardware. Axial position was sensed using a linear displacement transducer (LVDT) mounted on the hydraulic ram in the frame's crosshead (model 244.11). Analog signal conditioning was performed in hardware before passing to the PCI-based, 12-bit analog/digital conversion board (PCI-6071-E, National Instruments). The axial position resolution was 0.0074 mm in a preset  $\pm 15.24$  mm range. Data were sampled at 1 KHz or faster.

One may note that the sensors on the MTS and MEG aimed to measure the end effector position (and therefore the tissue thickness) and the forces applied on the tissue are located at different places along their respective kinematic chains, starting at the actuator and ending at the end effector. However, given the kinematics and the dynamics of each chain, the sensors' readings were mapped from their locations to the devices' end effectors. Locating the MEG's position and force

sensors proximal to the end effector without altering the end effector itself was motivated by the desire to use standard surgical instruments in a typical surgical environment. Placing a sensor on the end effector that could survive the in-vivo environment while not significantly altering the tool's geometry and/or ability to be used in-vivo would be extremely difficult. Moreover, since the endoscopic tool remained unchanged it is possible to remove it completely from the MEG, sterilize it, and use it in a survival procedure.

#### 24.2.1.5 Experimental Protocol and Loading Conditions

Three-month-old female pigs (porcine Yorkshire cross) with an average weight of 37 ( $\pm 5$ ) kg were used as the animal models for the experimental protocol. The same animal model is used for training laparoscopic surgeons due to its similar internal abdominal organ anatomy to humans. Seven internal organs (liver, spleen, bladder, gallbladder, small and large intestines, and stomach) taken from 14 different pigs were tested in various testing conditions (in-vivo, in-situ, and *ex-corpore*). The MEG was used for testing all seven organs of six animals, whereas the MTS machine was used on four organs (liver, spleen, small intestine, and stomach) from three animals. The MEG was used in all conditions, while the MTS was obviously used for only *ex-corpore* testing. (The remaining animals were tested with some mix of condition and organ.) The in-vivo and in-situ experiments were recorded visually using the endoscopic camera, synced with force-deformation data, and recorded on digital video for off-line analysis and archival.

In-vivo tests were performed on a sedated and anesthetized animal as per standard veterinary protocols and typical for a laparoscopic training procedure at the University of Washington Center for Videoendoscopic Surgery, an AALAC-accredited facility. The abdomen was insufflated with CO<sub>2</sub> to a pressure of 11–12 mmHg, as typical in porcine MIS procedures. Three laparoscopic ports (10mm in diameter) were placed into the abdomen, which allowed access to all the organs to be tested as well as visualization of the tool tip by the endoscopic camera. In-situ tests were conducted under the same experimental conditions on the euthanized animal immediately postmortem. *Ex-corpore* testing was performed at the UW Applied Biomechanics Laboratory. For the organ harvesting, blood vessels to the organs were cut, and blood was free to drain and clot. Hollow organs were stapled and then cut to ensure any contents remained intact. The organs were kept moist with 0.9% saline solution and stored in an ice chest with ice packs. The *ex-corpore* testing took place in a climate-controlled room; the temperature was held at 22.7°C with a humidity of 22% during all the tests. During the *ex-corpore* tests, the tissues were constantly kept moist with sprays of saline solution; the organs were never frozen.

Cyclic and step strains were used as the two loading conditions for testing the various soft tissues. In addition to these two loading conditions, the tissues were tested to failure, defined by a tissue fracture, by both devices *ex-corpore*. The loading characteristics used as part of the experimental protocol were defined based on a

detailed analysis of the grasping action in laparoscopic surgery, as measured by the Blue DRAGON system [43]. Moreover, since laparoscopy, by definition, is performed in-vivo, collecting load-response data under similar conditions is paramount to reflecting the nature of these biological materials as presented to the surgeon clinically. Emulating surgical conditions as part of the experimental protocol guaranteed that models that were developed based on the collected data reflected the appropriate nature of these biomaterials for future applications, such as haptic virtual reality surgical simulators. This concept manifested itself profoundly in the experimental protocol design and execution.

One of the major deviations from a more common soft tissue biomechanical testing protocol was in regard to tissue preconditioning. Due to the viscous nature of soft tissues, their deformation response changes with each successive loading cycle [2]. A stable behavior can develop after several loading cycles, at which point the tissue has been “conditioned,” and its hysteresis loop is minimized. Conditioning a tissue before testing (referred to as “preconditioning”) often takes 10–20 cycles, depending on the tissue and the loading condition [2]. Since tissues are not preconditioned before being manipulated in surgery, first-cycle behavior is of great interest, as is steady-state behavior and the number of cycles to reach conditioning. No preconditioning was performed during this study. A new site (location on the organ) was used for each test regime to ensure the natural (unconditioned) state of the tissue was measured.

Initial tissue thickness was determined by the distance between the tool tips (or indenters) at the point of first contact. Each subsequent cycle used this same value, whether or not the tissue was actually in contact at this distance. This was done to observe any depressions left in the tissue after the previous compression.

The first type of load applied was a cyclic position (strain) waveform, in order to examine the tissues’ elastic stress-strain response. The constant velocity (triangle-shaped) strain signal was the cyclic loading profile of choice for the following reasons: (1) it allows controlled strain rate, (2) it facilitates tool-tip contact detection based on deviation from nominal velocity, (3) it has been used in previous studies. The second type of load applied was a single position (strain) step, in order to examine the stress-relaxation properties of the tissues. A viscous material exhibits an exponential decrease in the measured stress within the material while the strain is held constant. Analysis of measurements made with the Blue DRAGON [43] indicated that maximum grasp time during various surgical tasks was 66.27 s. The average maximum grasp time was  $13.37 \pm 11.42$  s, the mean grasp time was  $2.29 \pm 1.65$  s, and 95% of each subject’s grasps were held for less than  $8.86 \pm 7.06$  s. Based on these results, a short hold time (10s or less) could be used for loading the tissues. However, it is useful for modeling purposes to examine the relaxation over a longer period of time, in order to better characterize the behavior. For practical purposes, the step strain was held for 60 s at three different strain levels (in different tests), targeted between 42 and 60% strain. During the step strain tests, the MEG end effector was commanded to close as rapidly as mechanically possible. It is important to note that the entire organ under study remained intact throughout the experimental protocol. Although the compressive loads were

applied uni-axially on the various organs, the surrounding tissues of the organs themselves define the boundary conditions. These boundary conditions are fundamentally different from the boundary conditions of a sample of tissue removed (excised) from an organ. With such a sample either free boundary conditions or confined boundary conditions within a fixed geometry can be used. Setting such controlled boundary conditions is a common practice in material testing; however, keeping the organ intact better reflects the boundary conditions encountered during real surgery. These testing conditions imply that the results reported in this study refer to both structural *and* material properties of tissues, not just to the material properties. In addition to the loading and boundary condition, the testing location on the organs were limited to the organs' peripheries for both the MEG and the MTS. These testing locations were selected due to the fact that the Babcock jaws of the MEG were less than 3 cm long; it was impossible to test the interior bulk of the larger organs like liver and stomach with the MEG.

#### 24.2.1.6 Data Analysis: Phenomenological Models

Two fundamental approaches exist for developing models of soft tissue mechanical behavior: (1) constitutive, physical law-based models, such as strain energy function models; and (2) phenomenological models based on curve-fitting experimental data. The former approach leads to easier extraction of physical meaning of the parameters but may not have perfect fits with the acquired data. The latter approach has little or no physical relevance but may achieve excellent fits to the acquired data with potentially less computationally intensive functions. Due to the empirical emphasis of this study, a phenomenological modeling approach was used. In order to evaluate which of these methods should be selected, a series of candidate curves were defined and evaluated for their ability to fit a significant portion of the dataset accurately and consistently. The measures of fit that were examined were the mean, median, and standard deviation of both  $R^2$  (regression coefficient) and RMSE (root mean squared error).

#### Elastic Models

Eight functions were chosen to model the elastic characteristics of the tissue. In these equations, the engineering (nominal) stress ( $\sigma$ ) is defined to be the ratio of compression force ( $F$ ) applied on the tissue to the contact area ( $A$ ) – (24.1a). The engineering strain ( $\epsilon$ ) is defined as the difference between the initial thickness of the tissue ( $l_0$ ) under no load and the actual thickness under the compression load ( $l$ ) normalized with respect to the initial thickness. Each model assumes zero compressive stress ( $\sigma$ ) at zero strain ( $\epsilon$ ), and a positive stress at positive strain. Theoretically, compressive strain must be less than unity (1), since a value of 1.0 indicates the material has been totally compressed.

$$\sigma = \frac{F}{A} \quad (24.1a)$$

$$\varepsilon = \frac{l_0 - l}{l_0} \quad (24.1b)$$

The first function (24.2) to be examined is a basic exponential function, referred to as EXP. Various forms of this equation have been used by several researchers [2, 15, 18, 20, 29].  $\alpha$  and  $\beta$  are coefficients determined by curve-fitting the experimental data.

$$\sigma = \beta(e^{\alpha\varepsilon} - 1) \quad (24.2)$$

The second function (24.3) is an expansion of EXP, introducing a linear term and increasing the order of strain to  $\varepsilon^2$ . This equation was developed for this study and is referred to as EXP2. Again,  $\gamma$  is a coefficient obtained by curve-fitting experimental data.

$$\sigma = \beta(e^{\alpha\varepsilon^2} - 1) + \gamma\varepsilon \quad (24.3)$$

The third function (24.4) incorporates the inverse of strain and is referred to as INV. This equation introduces a vertical asymptote in the stress-strain relation. This asymptote must lie between  $\varepsilon = 0$  and  $\varepsilon = 1$ . There may be some physical relevance to the value of this strain asymptote: it may reflect the amount of fluid within the tissue that cannot be exuded, or the point at which the tissue becomes incompressible.

$$\sigma = \beta\left(\frac{1}{1 - \alpha\varepsilon} - 1\right) \quad (24.4)$$

The fourth function (24.5) is a uni-axial form of a Blatz-Ko model and is referred to as BLATZ. This equation was previously used to model the kidney and liver under compression loading [44].

$$\sigma = \frac{-\gamma}{\alpha + 1} \left( (1 - \varepsilon)e^{\alpha((1-\varepsilon)^2 - 1)} - \frac{1}{(1 - \varepsilon)^2} e^{\alpha\left(\frac{1}{1-\varepsilon} - 1\right)} \right) \quad (24.5)$$

The final functions (described by (24.6)) are polynomials with increasing order from second ( $i=2$ ) to fifth ( $i=5$ ). They are referred to as POLY2 through POLY5.

$$\sigma = \sum_{i=1}^n c_i \varepsilon^i \quad (24.6)$$

The derivative of a stress-strain function with respect to strain defines the material stiffness, or tangent modulus. A linearly elastic material's stiffness would be a constant, or Young's modulus. The derivative of an exponential stress-strain relationship is a function of its strain (e.g., the derivative of (24.3) with respect to strain results in (24.7)). The overall stiffness indicators defined for EXP2 are  $\beta \times \alpha$  and  $\beta \times \alpha + \gamma$ , which serve as useful scalars for roughly approximating overall stiffness of a material and allowing quick comparisons between materials.

$$\frac{d\sigma}{d\epsilon} = 2\alpha(\beta e^{\alpha\epsilon^2}) \epsilon + \gamma \quad (24.7)$$

### Stress Relaxation Model

Three functions were selected to model the stress-relaxation data. The first function (24.8) is a logarithmic function with two time constants [2, 15] that is referred to as RLOG:

$$\sigma(t) = -A \ln(t) + B \quad (24.8)$$

where

$$A = \frac{c}{1 + c \ln(\tau_2) - c \ln(\tau_1)}$$

$$B = A \left( \frac{1}{c} - \gamma + \ln(\tau_2) \right)$$

and  $\gamma$  is the Euler constant ( $\gamma=0.5772$ ). Curve-fitting experimental data results in  $\tau_1$  and  $\tau_2$  (time constants) and  $c$ .

The second stress-relaxation function (24.9) is a decaying exponential function with a single time constant [2, 18, 45, 46] that is referred to as REXP1:

$$\sigma(t) = 1 - a + ae^{-\frac{t}{\tau}} \quad (24.9)$$

with  $a$  being a curve-fit coefficient.

The third equation (24.10) is a decaying exponential raised to a power, with a single time constant. This function is referred to as REXP2.

$$\sigma(t) = \exp\left(\left(\frac{-t}{\tau}\right)^\beta\right) \quad (24.10)$$

## 24.2.2 *Micro Scale Biomechanics*

Compression stresses at magnitudes between 0 and 250 kPa were applied in vivo to porcine abdominal organs using a motorized endoscopic grasper. Test tissues were harvested after 3h, and tissue injury was measured from histological sections based on cell death, fibrin deposition, and neutrophil infiltration. Based on preliminary FE models [47], it was determined that the central portion of the compression site would have a uniform stress level. The central uniform region was chosen as the site of histological damage measurement in order to reduce variance from spatial stress variation.

## 24.3 Results

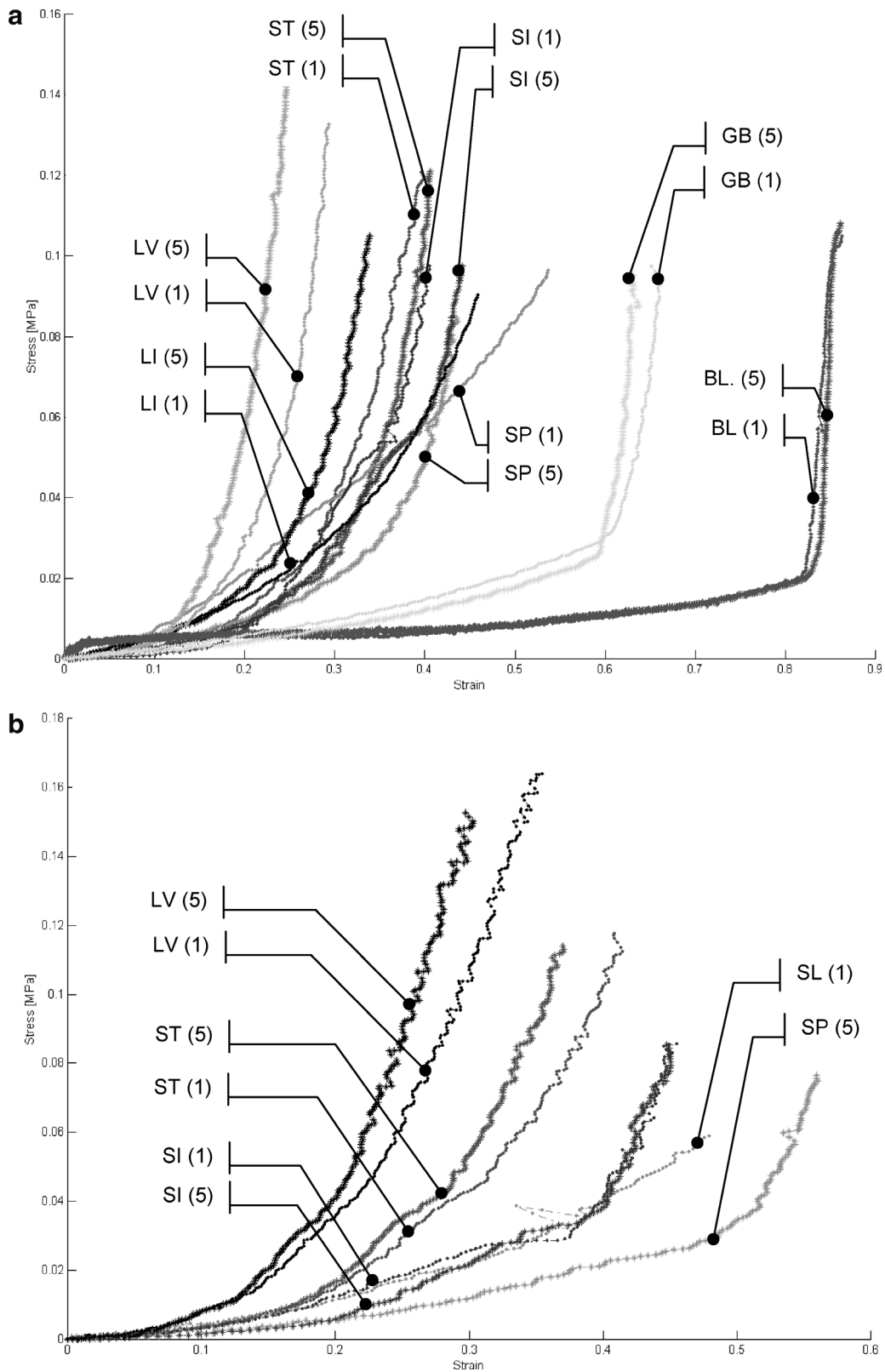
### 24.3.1 *Macro Scale Biomechanics*

#### 24.3.1.1 Elastic Testing

Compression stress-strain experimental data plots of various internal organs are depicted in Fig. 24.3 and the associated elastic phenomenological model (EXP, EXP2, and INV) curve fits are plotted in Fig. 24.4. Example organ response data, as well as the phenomenological models and their fit are plotted for the liver in Fig. 24.5. The average of the individual EXP2 model parameters across all conditions based on the MEG and MTS measurements in-vivo and *ex-corporis* are summarized in Table 24.1.

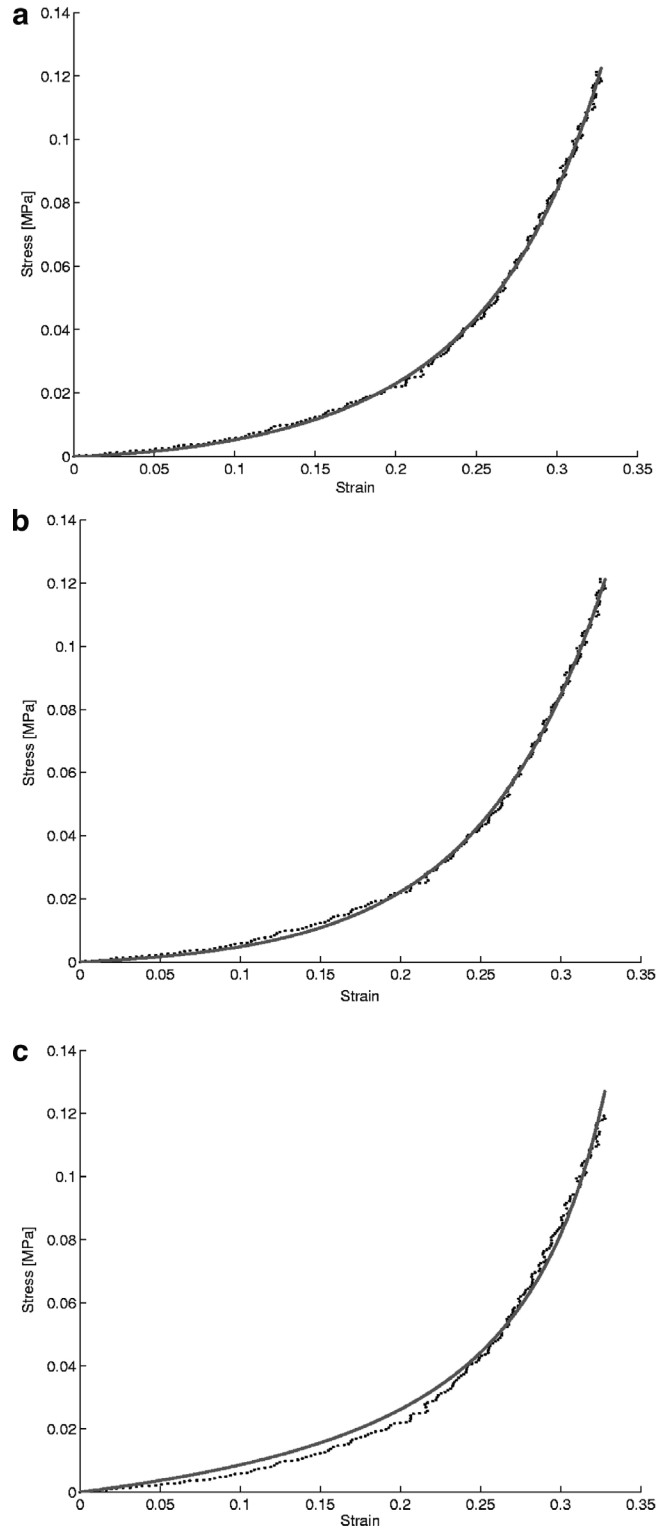
As indicated in Fig. 24.3, there is a major change in the stress-strain curve between the first and fifth loading cycles. Moreover, Fig. 24.3 depicts the spectrum of stress-strain characteristics bounded by the two extreme experimental conditions: (1) first cycle compression in-vivo – a typical loading condition during surgery (Fig. 24.3a), and (2) near-preconditioned fifth compression cycle *ex-corporis* – a loading condition more typical to biomechanical characterization analysis of soft tissue (Fig. 24.3b).

In general, it appeared that a tissue's stiffness increased with subsequent loading cycles for the first 7–10 loading cycles, at which point the stress-strain behavior reached a steady-state phase, indicating the point at which the tissue likely became conditioned. Note the marked difference in shape of the stress-strain curve between first and fifth loading cycles in spleen (Figs. 24.3 and 24.4). This behavior was noted visually during spleen testing by the fact that the MEG jaws tended to leave a deep impression in the organ after the first loading cycle; the tissue did not recover to its initial thickness after the first loading cycle. The spleen also appeared to have a nearly constant stiffness on first compression but became more exponential on subsequent cycles. The hollow organs, particularly small intestine, tended to have two distinct parts to their stress-strain curves, separated by an abrupt change in stiffness. The first part represents moving of the walls and compression of the



**Fig. 24.3** Stress-strain curves for all organs under study, as measured with the MEG at 5.4 mm/s loading velocity (first and fifth cycles shown): **(a)** in-vivo, **(b)** ex-corpore. Organs' legends: *BL* bladder, *GL* gallbladder, *LI* large intestine, *LV* liver, *SI* small intestine, *SP* spleen, *ST* stomach. The loading cycle number (1 or 5) is defined in the brackets

**Fig. 24.5** Measured data and phenomenological models of liver tissue under compression loading. The same in-vivo data measured by the MEG was fit with various models. The measures of fit for these models are: **(a)** EXP2,  $R^2 = 0.9989$ ,  $RMSE = 1.5048E3$ ; **(b)** EXP,  $R^2 = 0.9984$ ,  $RMSE = 1.5166E3$ ; **(c)** INV,  $R^2 = 0.9931$ ,  $RMSE = 3.0291E3$



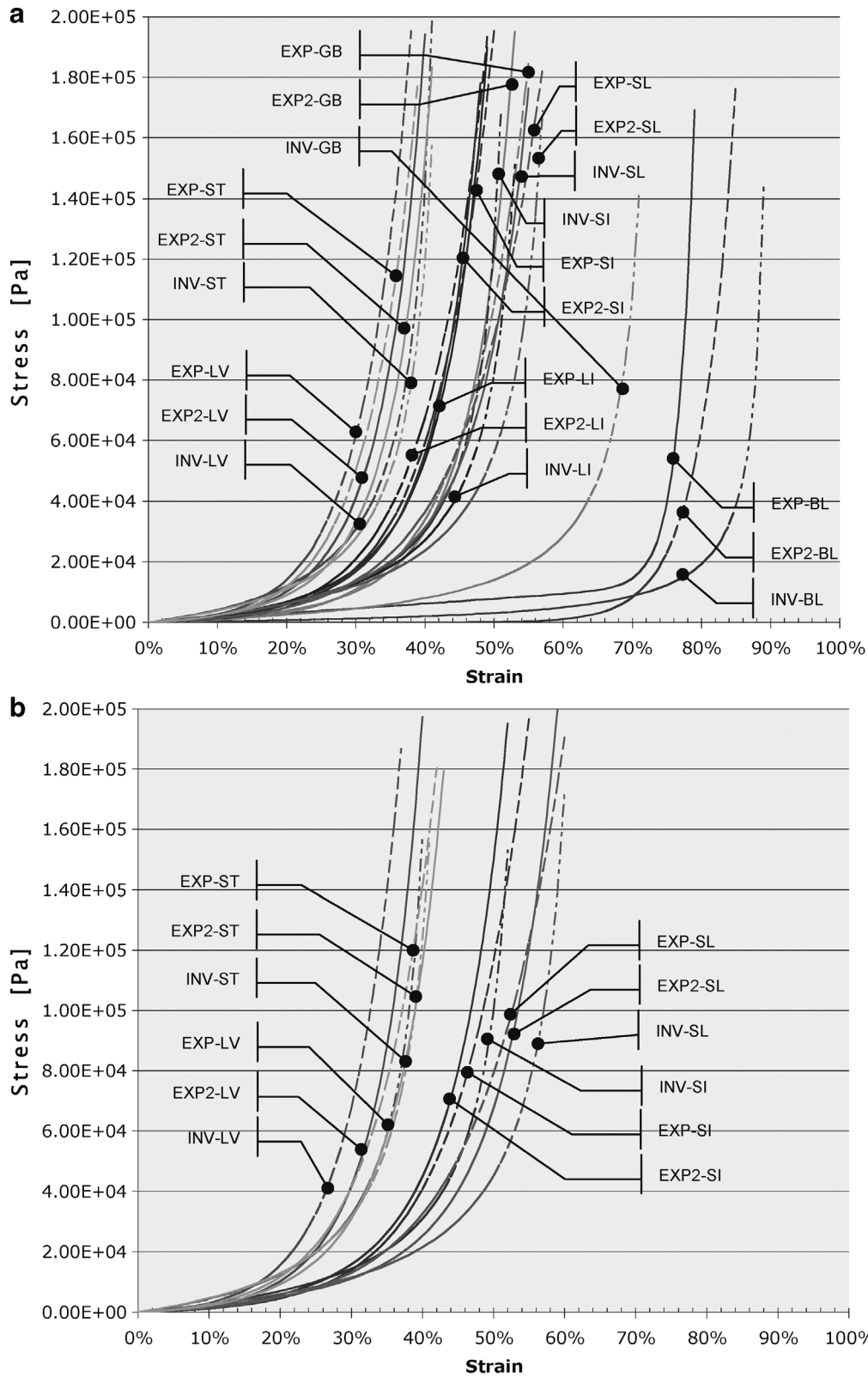


**Fig. 24.4** Stress-strain curves for all organs with average curve-fit parameters across all conditions: (a) in-vivo data measured by the MEG, (b) ex-corpus data measured by the MEG, (c) ex-corpus data measured by the MTS. Organ legend: *BL* bladder, *GL* gallbladder, *LI* large intestine, *LV* liver, *SI* small intestine, *SP* spleen, *ST* stomach. See text for the definitions of the functions EXP, EXP2, INV

**Table 24.1** Mean values of the EXP2 model parameters ( $\alpha$ ,  $\beta$ ,  $\gamma$ ) for each organ, in-vivo and ex-corpous, as tested by the MEG and MTS, across all animals, loading velocities, and cycle number

Device:	MEG			MEG			MTS		
Condition:	In-vivo			Ex-corpous			Ex-corpous		
Parameters:									
Organ	$\beta$ (Pa)	$\alpha$	$\gamma$ (Pa)	$\beta$ (Pa)	$\alpha$	$\gamma$ (Pa)	$\beta$ (Pa)	$\alpha$	$\gamma$ (Pa)
Bladder	0.0041	27.98	15,439.2	N/A	N/A	N/A	N/A	N/A	N/A
Gallbladder	2,304.5	15.75	9,622.2	N/A	N/A	N/A	N/A	N/A	N/A
Large intestine	3,849.7	16.14	16,544.1	N/A	N/A	N/A	N/A	N/A	N/A
Liver	7,377.1	20.63	3,289.4	7,972.1	20.29	781.0	8,449.8	26.26	1,679.4
Small intestine	3,857.3	16.60	11,273.8	6,166.5	12.81	7,967.5	1,745.9	13.60	2,580.9
Spleen	3,364.4	12.94	19,853.1	3,798.8	11.31	14,440.4	2,764.9	11.85	13,103.8
Stomach	4,934.9	21.51	11,105.9	8,107.0	16.91	6,483.8	2,247.6	21.22	6,803.3

contents (solid, air, or liquid). The second part occurs when the two walls of the organ contact each other. This portion, then, can be considered the actual deformation behavior of the *tissue* and should appear similar to the responses obtained by the other (solid) organs. One could argue the entire curve represents the clinically relevant behavior of the *organ*.

Large intestine response to loading was different than the small intestine, which could be attributed to its thicker walls and generally larger shape (Fig. 24.3a). However, because it contained stool, it tended to show drastically different biomechanical behavior between the first and subsequent squeezes as the contents were compressed and moved about. Small intestine tended not to have as much volume of contents as did the large intestine.

Two other hollow organs that show different behavior from the other organs, bladder and gallbladder, were fluid-filled. Therefore, their initial response was simply from the stretching of the membranous walls – more like tensile testing than compression. When the walls finally came together, because they were so thin, the jaws were essentially touching and the sudden change in stiffness to nearly rigid was observed (Fig. 24.3a). *Ex-corpous* results were generally similar to those seen in-vivo (Fig. 24.3b). For example, small intestine still had the two-part shape, and first-load cycle of spleen tended to be different from subsequent cycles. Ranges of stress and strain appeared to be similar, as well. One key difference was the amount of internal compression variability. Aside from the difference between first and second loading cycles, the stress-strain behavior reached a consistent response more quickly. This may indicate a more rapid onset of tissue conditioning, or it could be less influence from in-vivo factors such as ventilator motion and tissue re-perfusion.

### 24.3.1.2 Stress-Relaxation Testing

Experimental data of normalized stress-relaxation under compression loading are depicted in Fig. 24.6a for the liver. The stress was normalized with respect to

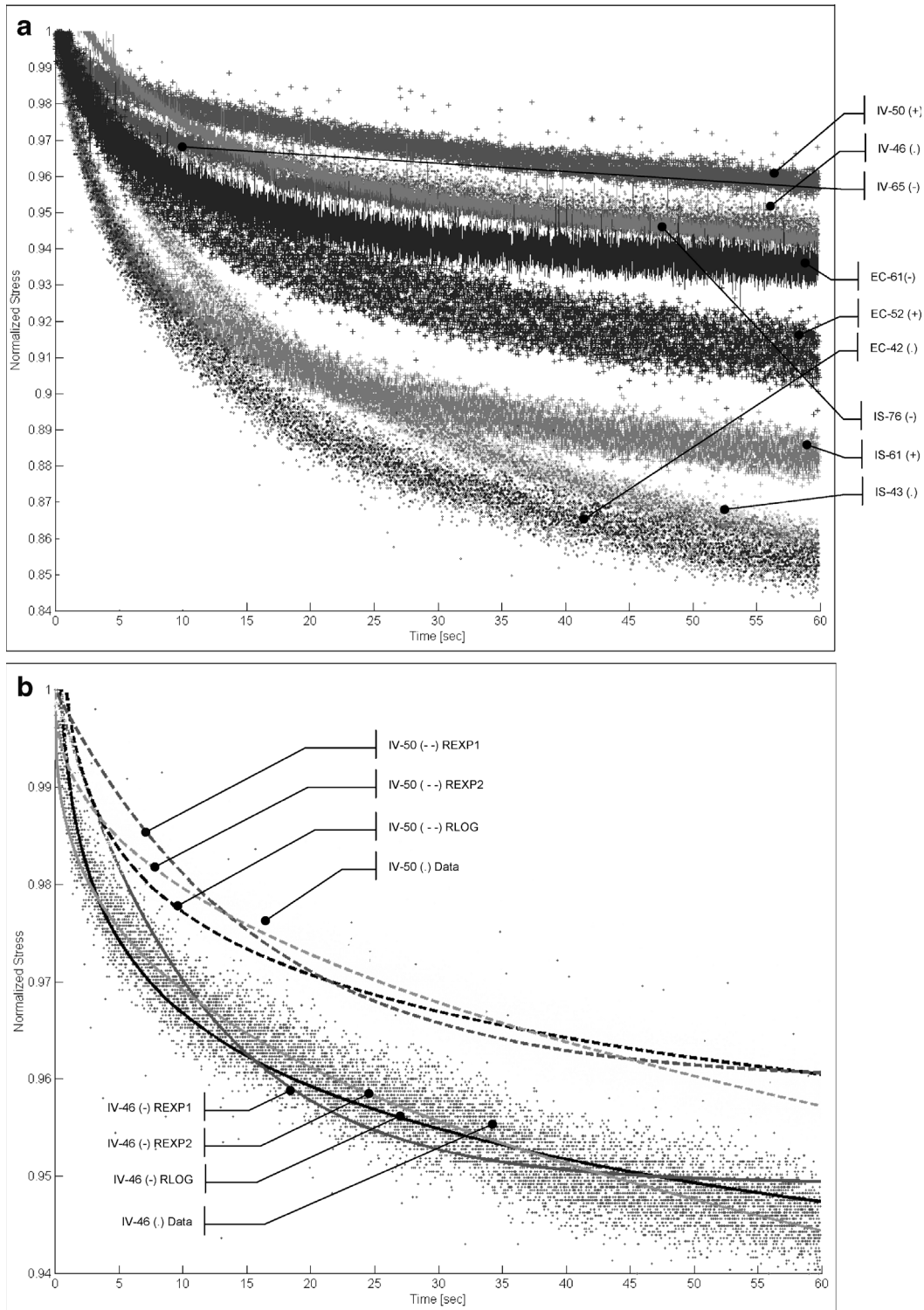


**Fig. 24.6** Normalized stress-relaxation curves as a function of time for one liver tested with the MEG: (a) three different testing conditions (*IV* in-vivo, *IS* in-situ, *EC* ex-corpore) and strain levels (indicated in the legends as a two-digit numeral [% strain]); (b) measured data and phenomenological models of two strain levels. Their measures of fit: 46% strain [REXP1 ( $R^2 = 0.8948$ ,  $RMSE = 0.0042$ ), REXP2 ( $R^2 = 0.9261$ ,  $RMSE = 0.0030$ ), RLOG ( $R^2 = 0.9084$ ,  $RMSE = 0.0034$ )], and strain 50% [REXP1 ( $R^2 = 0.9387$ ,  $RMSE = 0.0026$ ), REXP2 ( $R^2 = 0.9526$ ,  $RMSE = 0.0021$ ), RLOG ( $R^2 = 0.9140$ ,  $RMSE = 0.0028$ )]

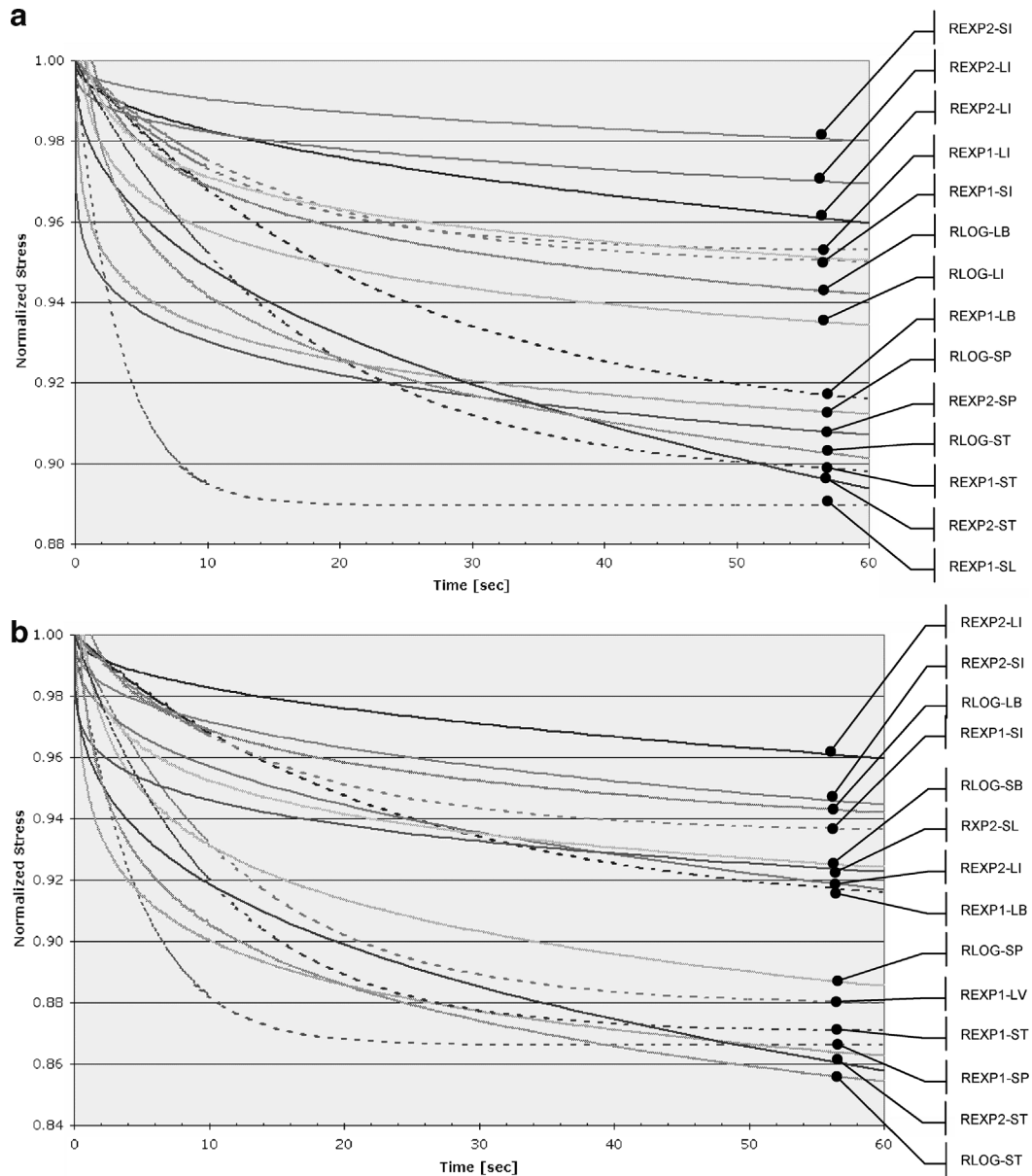


**Fig. 24.7** Average normalized stress-relaxation curves for internal organs, based on mean values of REXP1, REXP2, and RLOG models: (a) in-vivo, (b) ex-corpore. Organ legend: *BL* bladder, *GL* gallbladder, *LI* large intestine, *LV* liver, *SI* small intestine, *SP* spleen, *ST* stomach. See text for the definitions of the functions REXP1, REXP2, RLOG

the maximal value of the stress that applied during the loading phase. The associated phenomenological models (REXP1, REXP2, and RLOG) curve-fit functions are plotted in Figs. 24.6b and 24.7. The average of the individual REXP2 (the overall best fitting model) parameters across all conditions based on MEG and MTS measurements in-vivo and *ex-corpore* are summarized in Table 24.2.

The stress-relaxation data acquired from liver in-vivo and *ex-corpore* for various step strain levels are depicted in Fig. 24.6. The maximum value of the total decrease

**Table 24.2** Mean values of the REXP2 model parameters ( $\tau$ ,  $\beta$ ) for each organ, in-vivo and ex-corpore, as tested by the MEG and MTS across all animals, loading velocities, and cycle number

Device:	MEG		MEG		MTS	
Condition:	In vivo		Ex-corpore		Ex-corpore	
Parameter:						
Organ	$\tau$ (s)	$\beta$	$\tau$ (s)	$\beta$	$\tau$ (s)	$\beta$
Large intestine	4.72E+04	0.479	N/A	N/A	N/A	N/A
Liver	4.95E+06	0.307	3.71E+04	0.381	1.40E+00	0.233
Small intestine	7.87E+05	0.412	1.13E+05	0.380	N/A	N/A
Spleen	6.70E+07	0.167	1.10E+07	0.208	8.84E-01	0.188
Stomach	1.03E+04	0.425	1.73E+04	0.331	4.59E-01	0.189

in stress was about 4–6% over the 60s test in-vivo, while the in-situ and *ex-corpore* maximum total decreases were 6–14%. The data indicate three general trends: (1) greater percent decreases in stress in the in-situ and postmortem conditions compared to the in-vivo condition, (2) greater decrease in normalized stress with less applied strain, and (3) greater decrease in normalized stress with increasing time postmortem (in-situ versus *ex-corpore*).

### 24.3.1.3 Failure: Liver

One benefit of testing tissues postmortem is the ability to test them to failure. Failure for liver tissue was examined for MEG and MTS tests (Fig. 24.8). Tissue failure is indicated in Fig. 24.8 by an abrupt decrease in stress. Liver failed at 35–60% strain with the MEG and 30–43% strain with the MTS at stresses of 160–280kPa and 220–420kPa, respectively. These results compare favorably with previously collected data reporting ultimate strain for liver at  $43.8 \pm 4.0\%$  (range: 39.0–49.1%) and an ultimate stress of  $162.5 \pm 27.5\text{kPa}$  (range: 127.1–192.7kPa), when loaded at 5mm/s [15]. It is important to mention the difference in the boundary conditions between the two studies: in the study by Tamura et al. [15], rectangular samples were used rather than intact organs, as in this study. Some differences are therefore to be expected, but the orders of magnitude are similar, suggesting good agreement for both MEG and MTS results.

It was observed that failure mode was different for the MEG and MTS devices. The MEG, with its rounded and smooth jaw edges, tended to crush the internal structure of the liver, the parenchyma, a condition known as liver fracture. No damage to the outer capsule was visible, other than a depression. The indenter on the MTS machine, however, tended to tear the capsule before fracturing. This was likely due to the indenter's sharp edges and the sloping of the organ surface (Fig. 24.2).

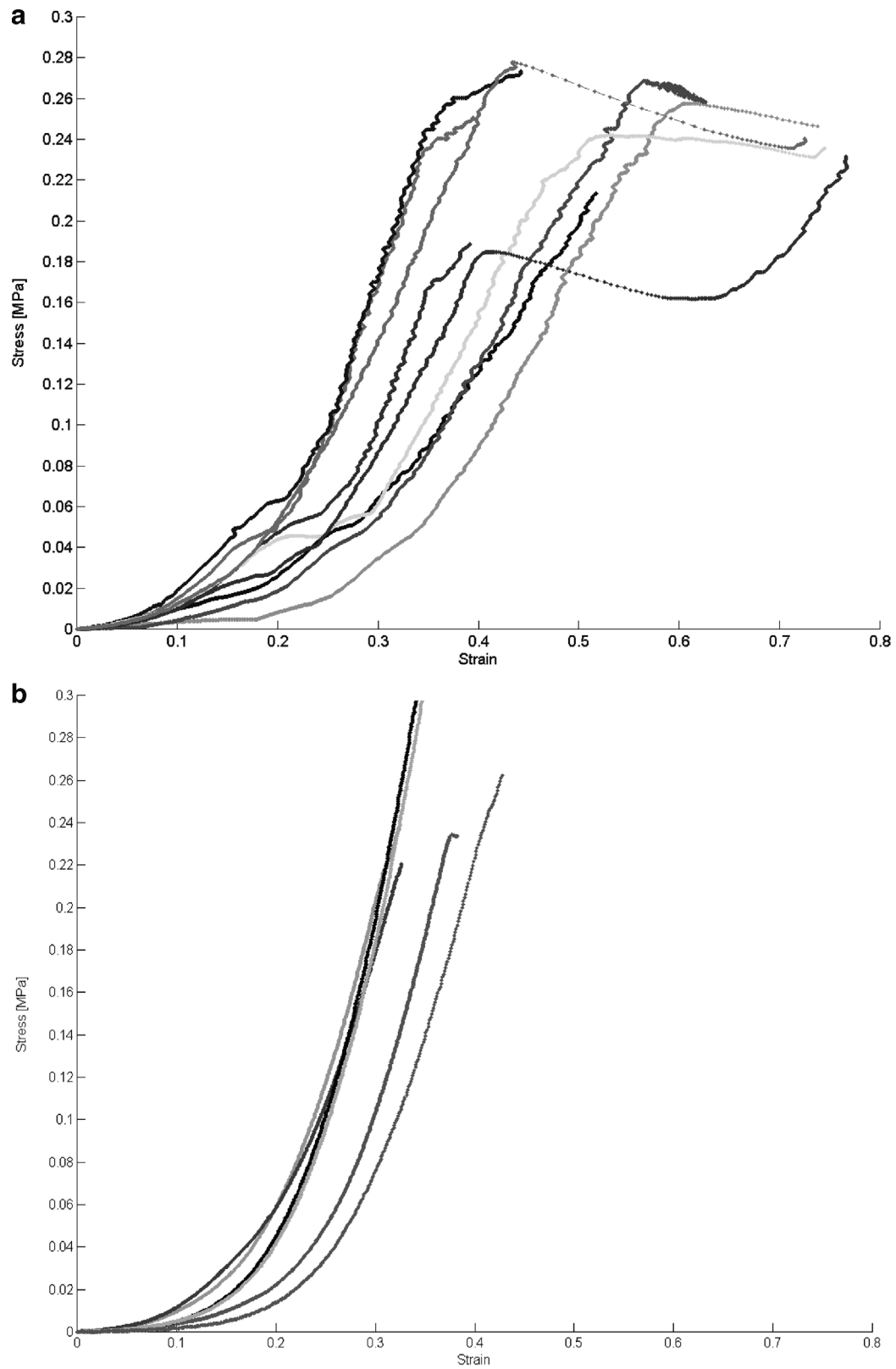


**Fig. 24.8** Ex-corpus stress-strain characteristics of the liver under compression loading to failure: (a) MEG, (b) MTS

**Table 24.3** The best fit of phenomenological models to the in-vivo experimental data acquired from various internal organs by the MEG under the two compression loading conditions (elastic stress-strain and stress relaxation) across all conditions

Organ	Data type	Model
Bladder	Elastic	EXP2
Gallbladder	Elastic	INV
Large intestine	Elastic	EXP2
	Relaxation	REXP2
Liver	Elastic	EXP2
	Relaxation	RLOG (REXP2)
Small intestine	Elastic	EXP2
	Relaxation	REXP2
Spleen	Elastic	EXP2
	Relaxation	RLOG (REXP2)
Stomach	Elastic	EXP2
	Relaxation	REXP2 (REXP2)

Models in parentheses are based on data acquired by the MTS system (ex-corpus only)

#### 24.3.1.4 Phenomenological Model Fit

Ranking the phenomenological models based on measures of fit (mean, median, and standard deviation of both R<sup>2</sup> and RMSE) separately and summing the ranks identified the best fitting model for each organ, summarized in Table 24.3. The phenomenological model parameters were identified for each set of acquired data (per organ, testing condition, cycle number, etc.). One may note that the hollow organs appeared to be fit best by REXP2, while the solid organs were fit best by RLOG.

#### 24.3.1.5 Statistical Analysis of phenomenological Model Parameters

One-way ANOVAs were performed for each factor-measure combination, with a probability value of 95% ( $\alpha=0.05$ ). In Figs. 24.9 and 24.10, each measure is plotted against the levels for each factor (such as organ or compression cycle). The diamonds represent the mean for a given level (e.g., liver is a level of the factor organ), and the horizontal bars indicate the standard deviation. The black dots are the individual data points. The right-hand side of the plots depict the results from post hoc Tukey-Kramer HSD (Honestly Significant Difference) analysis, as performed in the statistical software JMP (Cary, NC). This statistical test finds which pairs of levels have significantly different means, which is represented graphically by the circles: the center of each circle lies at the mean with the radius of the circle encompassing the region of confidence. If two circles overlap, then their means may not be significantly different and vice versa. The circles simply serve as a means for rapidly visually identifying significantly different groups.

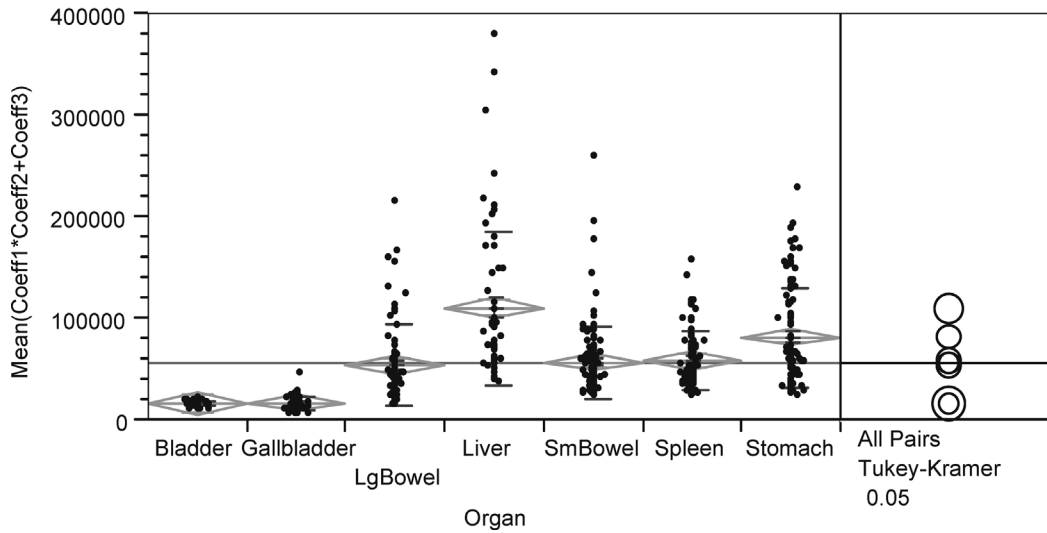


**Fig. 24.9** The stiffness indicator scalar  $b \times a + g$  of the EXP2 phenomenological model plotted for various organs for measured elastic data. The right-hand side of the plot depicts the results from post hoc Tukey-Kramer HSD analysis. The radius of the circle represents the region of confidence (95%)

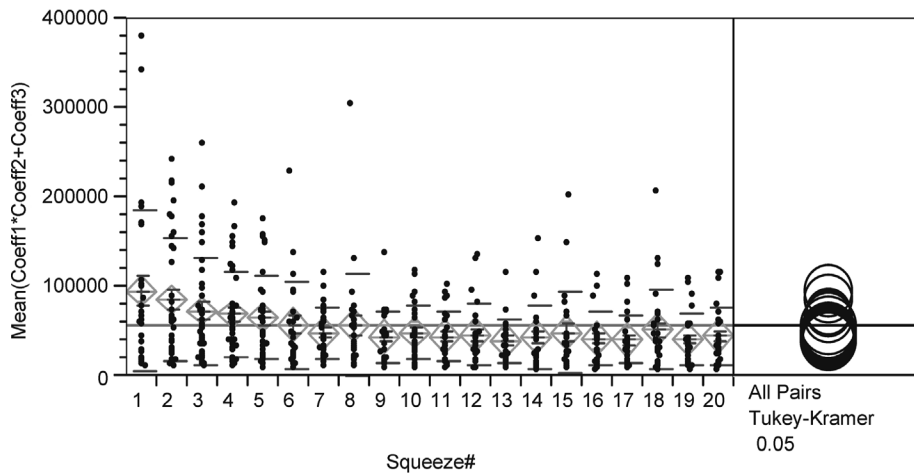


**Fig. 24.10** The stiffness indicator scalar  $b \times a + g$  of the EXP2 phenomenological model plotted as a function of loading cycle for measured elastic data. The right-hand side of the plot depicts the results from post hoc Tukey-Kramer HSD analysis. The radius of the circle represents the region of confidence (95%)

Using the general stiffness indicator scalar  $\beta \times \alpha + \gamma$  derived from (24.7) as a single indicator of the phenomenological model, a significant difference ( $p < 0.0001$ ) was found between the organs, indicating a significant difference in “stiffness” between the most of the organs. Only 4 of the possible 21 organ pairs were not found to be significantly different: spleen and small intestine, spleen and large intestine, small intestine and large intestine, and bladder and gallbladder (Fig. 24.9).

It is interesting to note that small and large intestine were not significantly different from each other using the overall stiffness measure ( $\beta \times \alpha + \gamma$ ). Only when looking solely at the  $\gamma$  term does one find a significant difference. This would indicate that the overall behavior of the intestines is similar, especially at higher strains, but their behavior is significantly different at low strains.

There was a significant difference ( $p < 0.0001$ ) found between loading cycle with respect to stiffness indicator scalar  $\beta \times \alpha + \gamma$  (Fig. 24.10). The stiffness indicator scalar for the first loading cycle was significantly greater than the seventh loading cycle and cycles 9–20. Moreover, the stiffness indicator scalar of the second loading cycle was greater than that from the 13th, 16th, 17th, and 19th loading cycles. These results indicate that the stiffness indicator scalar in the first six loading cycles is generally larger than latter loading cycles. A stable condition appears to be reached after 7–9 loading cycles.

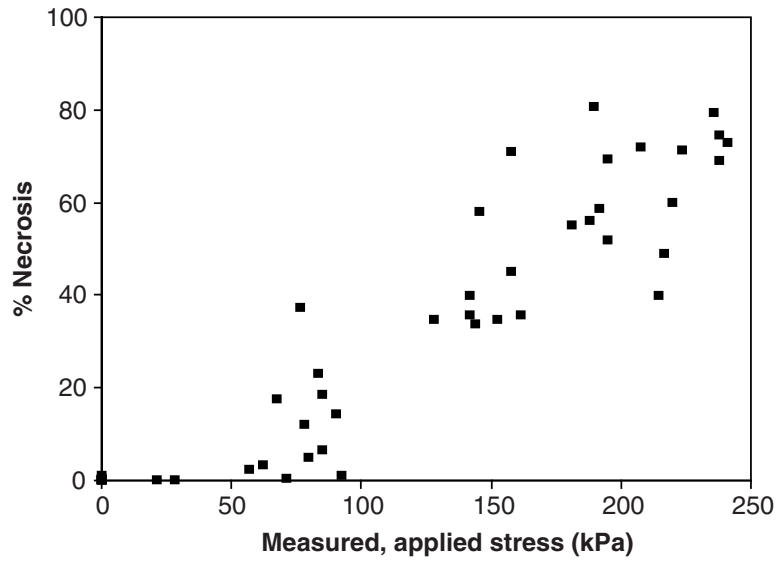
Statistical analysis of the models' parameters indicated several significant differences as the function of the testing conditions (in-vivo, in-situ, and *ex-corpore*).

### 24.3.2 *Micro Scale Biomechanics*

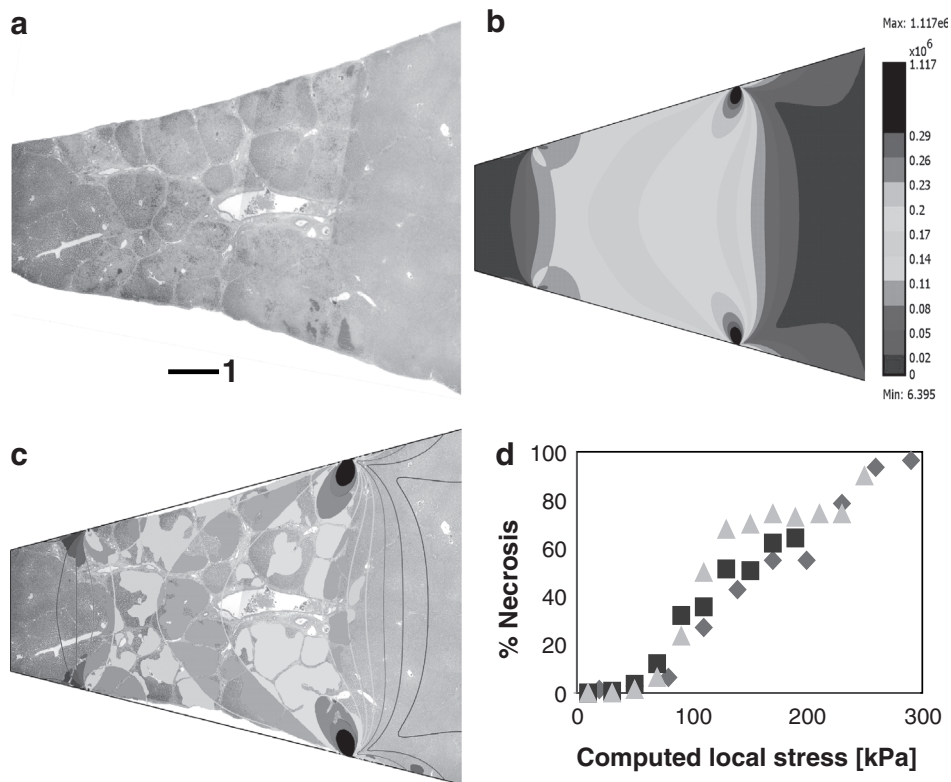
Histological analyses and tests showed that the sites of compression injury in the porcine liver exhibited early signs of hepatic necrosis in hematoxylin and eosin (H&E) stained sections. Figure 24.11 shows a plot of percent necrosis versus average applied stress based on 48 liver tissue samples from nine animal experiments. The results indicate a graded acute injury response to compression stress in the range of stresses typical to MIS.

Figure 24.12a is a composite of several microphotographs showing an H&E stained section of liver from the aforementioned animal after an applied compression stress of 200kPa. A finite element models (FEM) corresponding to the histological sections experiments was developed and depicted in Fig. 24.12b. The tissue was assumed to be linear, isotropic, and homogeneous. The Young's modulus equal to 300kPa was chosen based on previous measurements in relevant stress ranges [Sect. 3.1]. Poisson's ratio was set at 0.4, reflecting the nearly incompressible nature of soft tissues [48–50]. The two-dimensional FEM model was used to simulate the center plane of the grasping site, which was a plane of symmetry of the three-dimensional geometry and analogous to the histological sections. The mesh consisted of six-noded triangular elements.

An overlay of the computed von Mises stress contour lines of the FE model and the H&E section is presented in Fig. 24.12c. Most evident when comparing the histological section and FEM is the correlation between the high stress concentrations at the corners of the compression site in the model and the sites of hemorrhage in the tissue. The colored lines indicate the different stress levels in regular increments. The areas in which histology indicates early necrosis were colored manually in a solid color, with a different color used for each contour band. Any



**Fig. 24.11** Plot of necrosis in section images as a function of applied stress in the liver. Each data point is the average of four measurements



**Fig. 24.12** (a) H&E section of liver. (b) FE model of liver during vertical grasping. Plot shows von Mises stress with color bar indicating stress magnitude. (c) Overlay of FEM and HE section with marked necrosis. (d) Plot of necrosis versus damage based on three FEM-HE section overlays. Each shape indicates data from different section

large space void of hepatocytes, such as that formed by a large blood vessel, was subtracted when calculating percent damage. This analysis was repeated using two different histological sections from two additional animals (not shown). Figure 24.12d is a plot of percent necrosis by level of stress, as indicated by the contour bands, for the three analyzed sections.

It was expected that the central region of each compression site with the uniform stress to be uniformly damaged. However, upon closer inspection, there was clear spatial variation in necrosis within the lobules. This was seen in almost all histological sections.

In light of these results, a small scale FEM was developed to explore if the variations in damage within the compression region, which is theoretically under uniform stress is due to the microstructure of liver. The micro scale FEM represent  $2.94\text{mm} \times 2.2\text{mm}$  section of a (Fig. 24.13a). The pressure applied on this H&E stained section was 90kPa (compression – grasping). A magnified region from the center of the section is shown in Fig. 24.13b with six lobules from the center of the compression site chosen for the FEM outlined in blue. The identified regions of necrosis are outlined in green, illustrating the typical irregular patterns of damage within lobules.

The mesh of the microscopic model is seen in Fig. 24.13c and utilized six-node triangular elements. Similar to the global model, the local model was two-dimensional and assumed linearity and isotropy. Boundary conditions, or displacement inputs, for the local model were based on the x- and y- displacements calculated in the global model for a box corresponding to the position and outer dimensions of the local model. The Young's moduli of the stroma and hepatocytes were based on previous measurements of stress-strain characteristics of in vivo bulk liver. The hepatic tissue was assigned a linear approximation for Young's modulus of 160kPa [Sect. 3.1]. This is lower than the Young's modulus used for the first model (Fig. 24.12) because tissues have a lower linearly approximated stiffness at lower stresses. The stroma was given a higher Young's modulus of 1.6MPa to reflect higher values for collagen, a component of the stroma [51]. The Poisson's ratio for hepatocytes was kept at 0.4, but the value for lobular walls was reduced to 0.2, again to reflect lower Poisson's ratio values found in the literature for collagen [51].

One clear observation from these plots was that this model of microscopic tissue heterogeneity produced only small variations in stress and strain distributions within each of the lobules. Figure 24.13d shows the von Mises stress contours when the Young's modulus of the stroma was assumed to be one order of magnitude stiffer than the hepatic tissue. A direct comparison of the simulation results in the form of von Mises stress (Fig. 24.13d) or other aforementioned types of stress to histological results (Fig. 24.13b) did not show a match between higher areas of stress and areas of necrosis. This mismatch may be explained by the composite nature of the soft tissue and the small scale in which the stiff structure shielded the stress from the softer structures.

The Young's modulus used to characterize the stroma was simply an estimate since there have been no separate measurements on the two specific material types. Therefore, a parametric analysis (where the simulation is run several times while altering the value of one variable over a range) was employed to alter the Young's modulus of the stroma compared to the hepatocytes. This allowed to both confirm that the model was

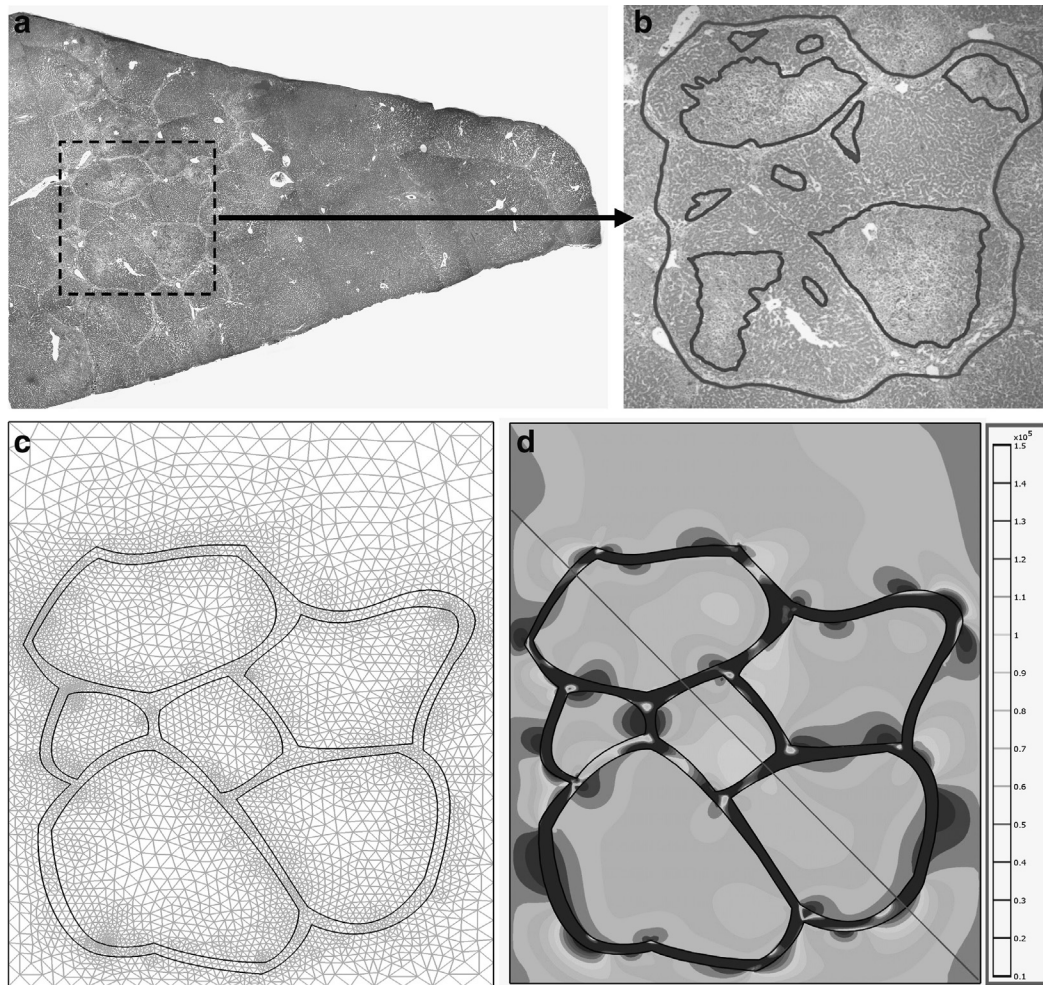


**Fig. 24.13** (a) H&E stained section of liver after 90 kPa applied compression stress. Box approximates boundaries for group of lobules shown in (b). (b) Blue line delineates lobules used to create microscopic FE model. Green indicates regions indicating early necrosis. (c) Mesh of FE lobule model (a finer mesh was used for the final analysis). (d) von Mises stress plot with contour band values given along the right (red = higher stress; blue = lower stress)

stable and to determine if observations regarding stress variations changed greatly with different Young's moduli. A plot of von Mises stress along a diagonal cross-sectional line through the lobule model (indicated by the red line in Fig. 24.13d) at various levels of Young's moduli is given in Fig. 24.14, with "spikes" or "dips" representing the connective tissue between lobules. The hepatocyte material property had a constant Young's modulus of 160kPa, while the connective tissue Young's modulus varied between 16kPa and 1.6MPa. Results from the parametric study suggested that variation of Young's modulus between the stroma and hepatocytes affected the magnitude of stress contours, but only small variation existed *within* lobules with spikes resulting at the stromal boundaries. This is further exemplified by the line  $E = 1.6 \text{ e}5$  in that small "spikes" still result when the only difference in the two materials is in the Poisson's ratio.

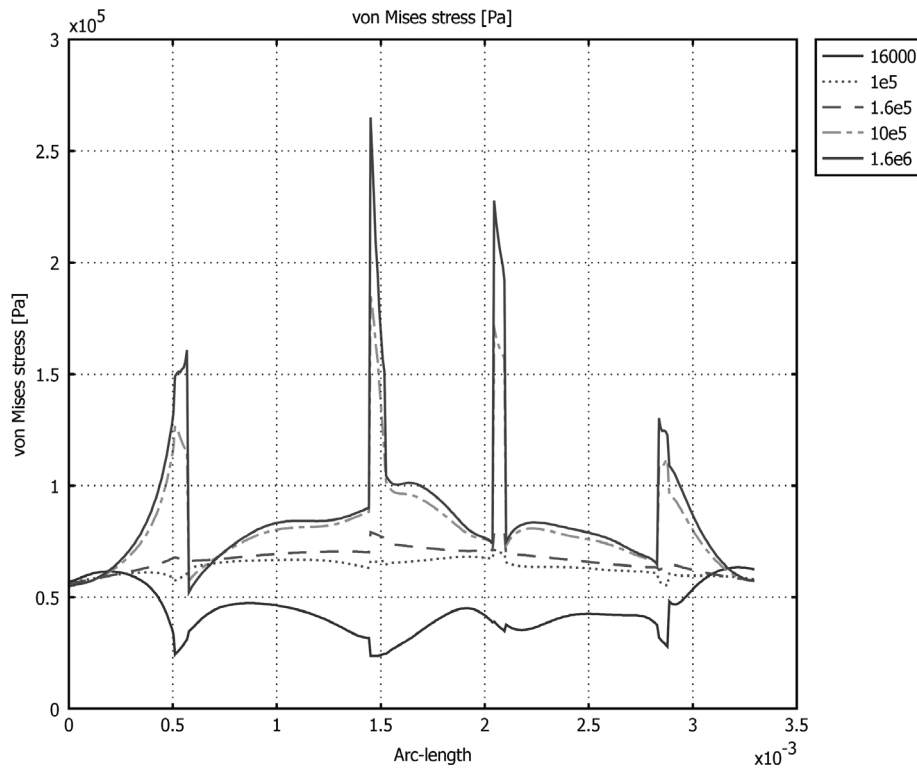


**Fig. 24.14** Plot of von Mises stress through diagonal (*red line* Fig. 24.13d) for parametric analysis altering stromal Young's modulus over range indicated by legend

Initial inspection of these results suggested that inclusion of heterogeneity in a finite element model resulted in stress variations that might be able to explain the irregular damage patterns observed in experimental sections. However, closer scrutiny showed that the stress and strain variations within the lobules, as exemplified by von Mises stress plots in Fig. 24.14, were quite minimal regardless of the assigned Young's moduli. The maximum variation within a lobule generally appeared to be 20–30 kPa. This range was essentially “flat” compared to the entire stress profile. A comparable analysis for a different histological section from another animal produced similar results, suggesting that either stress is not directly correlated to damage at this microscopic level or that FE modeling as a method for predicting damage at this level most-likely requires inclusion of more complex properties, both biological and structural.

## 24.4 Conclusions and Discussion

Structural biomechanical properties (stress-strain and stress-relaxation) of seven abdominal organs (bladder, gallbladder, large and small intestine, liver, spleen, and stomach) have been obtained using a porcine animal model. The organs were tested

in-vivo, in-situ, and *ex-corpore* under compressive loadings using a novel device, the Motorized Endoscopic Grasper (MEG), and a standard universal material testing system (MTS). The tissues were tested with the same loading conditions commonly applied by surgeons during minimally invasive surgical procedures. Phenomenological models were developed for the various organs, testing conditions, and experimental devices. The results indicate significant quantitative differences between tissue properties measured in-vivo and postmortem conditions that will be of value for developing performance criteria for the next generation of surgical robots and simulators.

One of the most difficult aspects of any testing of biological materials is the large degree of variability (difference between animals, heterogeneity of the organs, strain history-dependence, strain rate-dependence, etc.). This particular study compounded this problem by testing bulk organs in-vivo and without preconditioning. Testing tissues in-vitro, using specimens of known shape under very controlled loading and boundary conditions, can usually lead to results with lower variability, particularly if the tissues are preconditioned. Testing in-vivo also introduces potential sources of noise, such as movement artifacts from beating heart and respiration, varying rates of tissue re-perfusion, etc. Unfortunately, this variability may mask effects from other factors. Some of this might have been quantified by repeated testing of the same site, but the fact that the tissues exhibit strain history-dependence makes this impractical: the sites would have to be allowed to fully recover to their natural state before subsequent testing, requiring the animal to be anesthetized for extended amounts of time. While this variability makes finding statistical significance in the data difficult, for the scope of surgical simulation, it is worthwhile to determine ranges of tissue properties.

With this information, simulators can realistically change the organs' virtual mechanical behavior so that the virtual liver operated on in one session would be different from the next. Providing realistic force magnitudes identical to those felt by surgeons when grasping organs during actual surgery is the first step towards more realistic and scientifically-based surgical simulators incorporating haptic feedback. In addition, surgical instruments and surgical robot manufacturers can use this information for optimizing their products to provide sufficient grasping traction while minimizing trauma. This could decrease costs and improve patient outcome.

The goodness of fit measures of the phenomenological models to the experimental data are based on residual error. In the case of the elastic tests, residual error is typically highest at large strains, where small changes in strain cause rapid increases in stress. Therefore, the best fitting curves are often the ones that fit best in the large strain region (the steepest part of the curve) but may or may not fit as well at lower strains. Study of the stress-strain database shows that nearly any set of data can be fit well by a sufficiently high-order equation. However, this becomes unwieldy and physically irrelevant. Due to the large number of parameters in POLY4 and POLY5 and the fact that the functions are not monotonically increasing, these models are not the model of choice for internal organ soft tissues, despite their good measures of fit. Moreover, the functions POLY2 and POLY3 and BLATZ lacked sufficient goodness of fit. The INV and EXP2 models provided

better results than EXP, which is a curve commonly used by soft tissue studies. The EXP model may be better suited for tensile experiments, where there is no vertical asymptote before failure. Due to the nature of compression, strain varies from 0 to 1 and can never reach unity (1). For bulk materials that have not failed, there will always be a strain asymptote between 0 and 1. INV provides this number explicitly by its  $\beta$  term: the asymptote occurs at  $\varepsilon=1/\beta$ . This may shed some physical insight into the nature of the tissues. Perhaps this value of  $\beta$  represents the thickness of the fluid within the tissue that cannot be exuded, thus leading to an incompressible state. While EXP2 does not provide this physical information and has three parameters instead of two, it overwhelmingly is the best fitting of all the exponential-type functions and the best fitting of all functions under study.

Fitting models to stress-relaxation tests are highly dependent on the duration of the test. Extrapolation beyond the testing may lead to inaccurate results. Only the REXP1 model, of the three models examined, has a stress asymptote (of value  $1-a$ ), which is usually what is observed in tissue. Soft tissues are generally considered viscoelastic, which means there is some elastic component and a viscous component. After infinite time in compression, little stress is developed in the viscous component, and only the elastic component will remain, which is a finite, nonzero value. Models such as REXP2 and RLOG lack the asymptotic behavior as contained in REXP1. Therefore, extrapolating data based on these two models may predict non-physical behavior in which the stress continually decreases as a function of time, even beyond a value of zero – a physical impossibility. Despite this, REXP2 was overwhelmingly the best fit model to the data.

Analyzing the models' parameters of all the tissues under study that were tested with the MEG across the various conditions (in-vivo, in-situ, and ex-corpus) indicated the following characteristics. Given the elastic model EXP2 ((24.3) and (24.7)), the parameter  $g$  decreased significantly ( $p < 0.0068$ ) as a function of the time postmortem. The parameter  $g$  represents the linear portion of the stress-strain curve, which dominates the stresses generated at low strains. Therefore, the results indicate that lower stresses were developed for small strains postmortem as opposed to in-vivo. The stiffness indicators  $b \times a$  and  $b \times a + g$  were significantly increasing ( $p < 0.0001$ ) as a function of the time postmortem. The results of the stress-relaxation tests indicated that the tissue recovery between successive periodic step stains was greater for longer rest periods and for in-vivo. These phenomena can be explained in part by the higher perfusion of pressurized fluids within the tissues in-vivo, which may also contribute to the greater relaxation of the tissue postmortem than in-vivo. Despite the variability in the data, this study is a first step towards characterizing the highly complex behavior of abdominal soft tissues in their in-vivo state. The MEG is a useful and effective device capable of measuring compressive structural properties of abdominal tissues under in-vivo and surgically realistic conditions.

A full experimental characterization of a non-linear, fluid-perfused, non-isotropic material such as the major internal organs in-vivo is a complex endeavor. Proper modeling of bulk materials requires knowledge from tri-axial testing that can only come from tissue biomechanical studies that are not similar to surgical conditions.

The aim of this experimental protocol is to characterize the tissues' response to typical loading conditions in minimally invasive surgery. In that respect, the results reported in this study represent only one axis (dimension) of the tissue's tri-axial response. However, it should be emphasized that given the inherent dependencies between the three dimensions, the two unloaded dimensions are reflected in the dimension under study here. In addition, the dimension under study is the very same dimension that the surgeon is exposed to as he or she palpates the tissue with standard surgical tools. Moreover, one may note that one underlying assumption of the elastic model was that the compression stresses are zero at zero strain. This initial condition limits the reported elastic model to incorporate the soft tissues' residual stresses due to hydration and natural internal boundary conditions which in turn limits the model to accurately predict the tissues' stress response to small strains. This limitation is diminished for large strains, which are what surgeons typically apply during tissue manipulation.

Better understanding of the tool-tissue interface in MIS can lead to development of safer and more effective surgical instruments, and this may allow to overcome some of the limitations of novel MIS devices. Comparison of FE models corresponding to tissue sections subjected to compressive stress *in vivo* produced damage-stress relationships (Fig. 24.12d) similar to that obtained from analysis of multiple samples from multiple animals (Fig. 24.11), suggesting that FEM can predict tissue damage at a macroscopic level (centimeter scale). There are several implications of this result. First, FEM could be used for surgical instrument design by modifying tools to apply favorable stress distributions to tissue to reduce the potential for injury. Second, surgical simulators that utilize FEM modeling could provide feedback to trainees regarding tissue damage based on computed stress levels and extended data analogous to Fig. 24.12d. Finally, tissue damage could be minimized during a procedure through advanced treatment planning or improved control algorithms in surgical robots.

The liver has a highly complex, yet variable system of blood vessels and ducts as well as a dual blood supply (hepatic and portal). In addition, there are functional differences within the organ that may result in variation in oxygenation or metabolic burden. Incorporation of such biological and structural intricacies into an FE model could help provide a more complete understanding of tissue during surgical grasping.

Stress computed by homogeneous FEM of surgical grasping of liver correlated with damage seen in experimental tissues at a macroscopic level. This relationship was observed both by taking multiple tissue samples from multiple animals as well as by comparing single histological sections to their corresponding computed stress profiles. Microscopically, we did not see a similar correlation, which suggests that incorporating three dimensions or other anatomical and physiological effects in microscopic simulation models may be required to better predict tissue damage at that scale.

## References

1. Madhani, A.J., Niemeyer, G., Salisbury, J.K. Jr.: The Black Falcon: a teleoperated surgical instrument for minimally invasive surgery. In: IEEE/RSJ International Conference on Intelligent Robots and Systems, New York, NY, 1998, vol. 2, pp. 936–944
2. Fung, Y.C.: *Biomechanics: Mechanical Properties of Living Tissues*, 2nd edn. Springer Verlag, New York (1993)
3. Fung, Y.C.: Elasticity of soft tissues in simple elongation. *Am. J. Physiol.* **213**(6), 1532–1544 (1967)
4. Yamada, H.: *Strength of Biological Materials*. Robert E. Krieger Publishing, Huntington, NY (1973)
5. Yoganandan, N., Pintar, F.A., Maltese, M.R.: Biomechanics of abdominal injuries. *Crit. Rev. Biomed. Eng.* **29**(2), 173–246 (2001)
6. Rouhana, S.W.: Biomechanics of abdominal trauma. In: Nahum, A.M., Melvin, J.W. (eds.) *Accidental Injury: Biomechanics and Prevention*, pp. 391–428. Springer-Verlag, New York (1993)
7. Liu, Z., Bilston, L.: On the viscoelastic character of liver tissue: experiments and modelling of the linear behaviour. *Biorheology* **37**(3), 191 (2000)
8. Arbogast, K.B., Thibault, K.L., Pinheiro, B.S., Winey, K.I., Margulies, S.S.: A high-frequency shear device for testing soft biological tissues. *J. Biomech.* **30**(7), 757–759 (1997)
9. Dokos, S., LeGrice, I.J., Smail, B.H., Kar, J., Young, A.A.: A triaxial-measurement shear-test device for soft biological tissues. *Trans. ASME J. Biomech. Eng.* **122**(5), 471–478 (2000)
10. Gao, C.W., Gregersen, H.: Biomechanical and morphological properties in rat large intestine. *J. Biomech.* **33**(9), 1089 (2000)
11. Gregersen, H., Emery, J.L., McCulloch, A.D.: History-dependent mechanical behavior of guinea-pig small intestine. *Ann. Biomed. Eng.* **26**(5), 850 (1998)
12. Carter, F.J., Frank, T.G., Davies, P.J., Cuschieri, A.: Puncture forces of solid organ surfaces. *Surg. Endosc.* **14**(9), 783–786 (2000)
13. Carter, F.J., Frank, T.G., Davies, P.J., McLean, D., Cuschieri, A.: Measurements and modelling of the compliance of human and porcine organs. *Med. Image Anal.* **5**(4), 231–236 (2001)
14. Davies, P.J., Carter, F.J., Cuschieri, A.: Mathematical modelling for keyhole surgery simulations: a biomechanical model for spleen tissue. *IMA J. Appl. Math.* **67**, 41–67 (2002)
15. Tamura, A., Omori, K., Miki, K., Lee, J.B., Yang, K.H., King, A.I.: Mechanical characterization of porcine abdominal organs. In: *Proceedings of the 46th Stapp Car Crash Conference, 2002*, vol. 46, pp. 55–69
16. Melvin, J.W., Stalnaker, R.L., Roberts, V.L., Trollope, M.L.: Impact injury mechanisms in abdominal organs. In: *Proceedings of the 17th Stapp Car Crash Conference, 1973*, pp. 115–126
17. Zheng, Y.P., Mak, A.F.T., Lue, B.: Objective assessment of limb tissue elasticity: development of a manual indentation procedure. *J. Rehabil. Res. Dev.* **36**(2) (1999)
18. Zheng, Y.P., Mak, A.F.T.: Extraction of quasi-linear viscoelastic parameters for lower limb soft tissues from manual indentation experiment. *J. Biomech. Eng.* **121**(3), 330–339 (1999)
19. Pathak, A.P., Silver, T.M.B., Thierfelder, C.A., Prieto, T.E.: A rate-controlled indenter for in vivo analysis of residual limb tissues. *IEEE Trans. Rehabil. Eng.* **6**(1), 12–20 (1998)
20. Brouwer, I., Ustin, J., Bentley, L., Sherman, A., Dhruv, N., Tendick, F.: Measuring in vivo animal soft tissue properties for haptic modeling in surgical simulation. *Stud. Health Technol. Inform.* **81**, 69–74 (2001)
21. Ottensmeyer, M.P., Salisbury, J.: In-vivo mechanical tissue property measurement for improved simulations. *Proc. SPIE* **4037**, 286–293 (2000)
22. Kalanovic, D., Ottensmeyer, M.P., Gross, J., Buess, G., Dawson, S.L.: Independent testing of soft tissue viscoelasticity using indentation and rotary shear deformations. In: *Medicine Meets Virtual Reality, Newport Beach, CA, 22–25 January*. *Stud. Health Technol. Inform.* **94**, 137–143 (2003)

23. Bicchi, A., Canepa, G., De, R.D., Iacconi, P., Scillingo, E.P.: A sensor-based minimally invasive surgery tool for detecting tissue elastic properties. In: Proceedings 1996 IEEE International Conference on Robotics and Automation, New York, NY, 1996, vol. 1, pp. 884–888
24. Morimoto, A.K., Foral, R.D., Kuhlman, J.L., Zucker, K.A., Curet, M.J., Bocklage, T., MacFarlane, T.I., Kory, L.: Force sensor for laparoscopic Babcock. In: Medicine Meets Virtual Reality, 1997, pp. 354–361
25. Greenish, S., Haywar0, V., Chial, V., Okamura, A., Steffen, T.: Measurement, analysis, and display of haptic signals during surgical cutting. *Presence Teleop. Virt. Environ.* **11**(6), 626–651 (2002)
26. Brown, J.D., Rosen, J., Longnion, J., Sinanan, M., Hannaford, B.: Design and performance of a surgical tool tracking system for minimally invasive surgery. In: ASME International Mechanical Engineering Congress and Exposition, Advances in Bioengineering, New York, 11–16 November 2001, vol. 51, pp. 169–170
27. Rosen, J., Brown, J.D., Barreca, M., Chang, L., Hannaford, B., Sinanan, M.: The Blue DRAGON – a system for monitoring the kinematics and the dynamics of endoscopic tools in minimally invasive surgery for objective laparoscopic skill assessment. In: Medicine Meets Virtual Reality, Newport Beach, CA, 23–26 January 2002. *Stud. Health Technol. Inform.* **85**, 412–418 (2002)
28. Rosen, J., Brown, J.D., Barreca, M., Chang, L., Sinanan, M., Hannaford, B.: The Blue-DRAGON – a system for measuring the kinematics and the dynamics of minimally invasive surgical instruments in-vivo. In: 2002 IEEE International Conference on Robotics and Automation, Washington, DC, 2002, vol. 2, pp. 1876–1881
29. Rosen, J., Hannaford, B., MacFarlane, M.P., Sinanan, M.N.: Force controlled and teleoperated endoscopic grasper for minimally invasive surgery – experimental performance evaluation. *IEEE Trans. Biomed. Eng.* **46**(10), 1212–1221 (1999)
30. Brown, J.D., Rosen, J., Moreyra, M., Sinanan, M., Hannaford, B.: Computer-controlled motorized endoscopic grasper for in vivo measurement of soft tissue biomechanical characteristics. In: Medicine Meets Virtual Reality, Newport Beach, CA, 23–26 January. *Stud. Health Technol. Inform.* **85**, 71–73 (2002)
31. Brown, J.D., Rosen, J., Kim, Y.S., Chang, L., Sinanan, M.N., Hannaford, B.: In-vivo and in-situ compressive properties of porcine abdominal soft tissues. In: Medicine Meets Virtual Reality, Newport Beach, CA, 22–25 January. *Stud. Health Technol. Inform.* **94**, 26–32 (2003)
32. Brown, J.D., Rosen, J., Sinanan, M.N., Hannaford, B.: In-vivo and postmortem compressive properties of porcine abdominal organs. In: MICCAI 2003, Montreal, Canada. *Lecture Notes in Computer Science*, 2003, vol. 2878, pp. 238–245
33. Mkandwire, C., Ledoux, W., Sangeorzan, B., Ching, R.: A quasi-linear viscoelastic model of foot-ankle ligaments. In: 25th Annual Meeting of the American Society of Biomechanics, University of California-San Diego, San Diego, CA, 8–11 August 2001
34. Woo, S.L., Simon, B.R., Kuei, S.C., Akeson, W.H.: Quasi-linear viscoelastic properties of normal articular cartilage. *J. Biomech. Eng.* **102**(2), 85–90 (1980)
35. Mow, V.C., Kuei, S.C., Armstrong, C.G.: Biphasic creep and stress relaxation of articular cartilage in compression: theory and experiments. *Trans. ASME J. Biomech. Eng.* **102**(1), 73–84 (1980)
36. Ateshian, G.A., Warden, W.H., Kim, J.J., Grelsamer, R.P., Maw, V.C.: Finite deformation biphasic material properties of bovine articular cartilage from confined compression experiments. *J. Biomech.* **30**(11/12), 1157–1164 (1997)
37. DiSilvestro, M.R., Suh, J.K.: A cross-validation of the biphasic poroviscoelastic model of articular cartilage in unconfined compression, indentation, and confined compression. *J. Biomech.* **34**(4), 519–525 (2001)
38. DiSilvestro, M.R., Qiliang, Z., Marcy, W., Jurvelin, J.S., Jun, K.F.S.: Biphasic poroviscoelastic simulation of the unconfined compression of articular cartilage: I-Simultaneous

- prediction of reaction force and lateral displacement. *Trans. ASME. J. Biomech. Eng.* **123**(2), 191–197 (2001)
39. DiSilvestro, M.R., Qiliang, Z., Jun, K.F.S.: Biphasic poroviscoelastic simulation of the unconfined compression of articular cartilage: II-Effect of variable strain rates. *Trans. ASME. J. Biomech. Eng.* **123**(2), 198–200 (2001)
  40. Fortin, M., Hat, J., and Hmann, M.D.: Unconfined compression of articular cartilage: nonlinear behavior and comparison with a fibril-reinforced biphasic model. *J. Biomech. Eng.* **122**(2), 189–195 (2000)
  41. Suh, J.K., Spilker, R.L.: Indentation analysis of biphasic articular cartilage: nonlinear phenomena under finite deformation. *J. Biomech. Eng.* **116**(1), 1–9 (1994)
  42. Lai, W.M., Hou, J.S., Mow, V.C.: A triphasic theory for the swelling and deformation behaviors of articular cartilage. *Trans. ASME. J. Biomech. Eng.* **113**(3), 245–258 (1991)
  43. Brown, J.R.: J.; Chang, L.; Sinanan, M.N.; Hannaford, B., Quantifying surgeon grasping mechanics in laparoscopy using the Blue DRAGON system. *Medicine Meets Virtual Reality. Stud. Health Technol. Inform.* **98**, 34–36 (2004)
  44. Farshad, M., Barbezat, M., Flueler, P., Schmidlin, F., Graber, P., Niederer, P.: Material characterization of the pig kidney in relation with the biomechanical analysis of renal trauma. *J. Biomech.* **32**(4), 417–425 (1999)
  45. Wang, J., Brienza, D.M., Bertocci, G., Karg, P.: Stress relaxation properties of buttock soft tissues: in vivo indentation test. In: *Proceedings of the RESNA 2001 Annual Conference, RESNA, Reno, Nevada, 22–26 June 2001*, pp. 391–393
  46. Simon, B.R., Coats, R.S., Woo, S.L.: Relaxation and creep quasilinear viscoelastic models for normal articular cartilage. *J. Biomech. Eng.* **106**(2), 159–164 (1984)
  47. De, S., et al.: Assessment of tissue damage due to Mechanical Stresses, *Int. J. Rob. Res.* **26**, 1159 (2007)
  48. Niculescu, G., Foran, D.J., Noshier, J.: Non-rigid registration of the liver in consecutive CT studies for assessment of tumor response to radiofrequency ablation. *Conf. Proc. IEEE Eng. Med. Biol. Soc.* **1**, 856 (2007)
  49. Brock, K.K., Sharpe, M.B., Dawson, L.A., Kim, S.M., Jaffray, D.A.: Accuracy of finite element model-based multi-organ deformable image registration. *Med. Phys.* **32**, 1647 (2005)
  50. Chui, C., Kobayashi, E., Chen, X., Hisada, T., Sakuma, I.: Transversely isotropic properties of porcine liver tissue: experiments and constitutive modelling. *Med. Biol. Eng. Comput.* **42**, 787 (2004)
  51. Sasaki, N., Odajima, S.: Stress–strain curve and Young’s modulus of collagen molecules as determined by the X-ray diffraction technique. *J. Biomech.* **29**, 655–658 (1996)